Check for updates

JGR Earth Surface

RESEARCH ARTICLE
10.1029/2026JF009300

Spatial Variation in Effective Pressure Beneath Thwaites Glacier, West Antarctica, Inferred From Seismic Data

Ronan S. Agnew[1], Sridhar Anandakrishnan[2], Alex M. Brisbourne[1], Kevin Hank[1], Atsuhiro Muto[3], Lucas K. Zoet[4], Louise Borthwick[3], Sierra M. Melton[2], Amanda Willet[2], Richard B. Alley[2], and Andrew M. Smith[1]

[1]British Antarctic Survey, Cambridge, UK, [2]Department of Geosciences, The Pennsylvania State University, University Park, State College, PA, USA, [3]Department of Earth and Environmental Science, Temple University, Philadelphia, PA, USA, [4]Department of Geoscience, University of Wisconsin-Madison, Madison, WI, USA

Key Points:

- We use wide-angle reflection seismic surveys to image subglacial topography and infer bed properties near Ghost Ridge at Thwaites Glacier
- The reflection from the ice base is consistent with a bed of spatially heterogeneous sediments with soft and stiff sediments present
- We constrain porosity and effective pressure with viscous grain shearing theory and infer that effective pressure varies over our profile

Correspondence to:
R. S. Agnew,
rognew91@bas.ac.uk

Citation:
Agnew, R. S., Anandakrishnan, S., Brisbourne, A. M., Hank, K., Muto, A., Zoet, L. K., et al. (2026). Spatial variation in effective pressure beneath Thwaites Glacier, West Antarctica, inferred from seismic data. *Journal of Geophysical Research: Earth Surface*, *131*, e2026JF009300. https://doi.org/10.1029/2026JF009300

Received 27 MAR 2026
Accepted 3 NOV 2026

Abstract Constraining the properties of subglacial materials is key to the accurate parameterization of glacial slip in ice sheet models and is therefore important for accurate projections of sea level rise. The bed properties of Thwaites Glacier are important because Thwaites is the second largest contributor to West Antarctica's mass loss, having contributed 1.8 mm of sea level rise between 1979 and 2017. Furthermore, mass loss from Thwaites Glacier is accelerating. We report the results of active-source seismic surveys undertaken during the 2023/24 Antarctic field season, immediately upstream of the subglacial ridge known as Ghost Ridge. These include a 14.4 km profile of normal-incidence data and wide-angle data over sections totalling ∼5 km. Estimation of basal acoustic impedance reveals that the bed in this region is composed of sediments, with regions of both soft and stiff sediments present. Amplitude-versus-angle (AVA) analysis of wide-angle data supports this interpretation, with soft bed regions displaying high Poisson's ratios (>0.45). We image bedforms that are interpreted as sedimentary depositional bedforms; one of these is a crag and tail formation, and the other appears as a sedimentary tail emerging from rolling topography upstream. The tails of these features are probably composed of soft till. We apply Viscous Grain Shearing (VGS) theory to results obtained from AVA analysis to constrain the porosity and effective pressure of the subglacial sediments. VGS analysis suggests that the changes in reflectivity along our seismic profile are controlled by changes in effective pressure at the ice base as well as porosity.

Plain Language Summary Knowledge of the types of materials existing underneath glaciers and ice sheets is important for building accurate ice sheet models and predicting sea level rise. This is because different materials provide different amounts of friction to the glacier bed and can more strongly or weakly resist flow. This is particularly important for Thwaites Glacier because this glacier is making a large contribution to Antarctica's ice loss. We surveyed an area of Thwaites Glacier thought to be important for its future stability using the reflection of seismic waves from the ice base. We image sedimentary landforms beneath the glacier, with a variation of smooth and rolling topography. We interpret from the strength of reflected signal that the bed here is composed of sediments, some of which are soft and some of which are stiff. We also investigate the likely pressure of water contained in sediments at the ice base to further understand influences on ice flow.

1. Introduction

Understanding the dynamics of the West Antarctic Ice Sheet (WAIS) is critical for projecting global sea level rise over the coming centuries. The rate of ice mass loss from WAIS has increased over recent decades. This is driven by changes in the Amundsen Sea Embayment, for which ice discharge increased 77% between 1973 and 2013 (Mouginot et al., 2014). The increase in mass loss has been attributed to higher rates of ice-shelf basal melting due to Circumpolar Deep Water intruding onto the continental shelf, a result of anthropogenically forced changes in wind conditions (Holland et al., 2019). The increased melt has caused a thinning and retreat of ice shelves exacerbated by melt-driven feedbacks (Holland et al., 2023) and an acceleration of the grounded ice (Seroussi et al., 2017; dos Santos et al., 2021). Grounding lines, where the ice begins to float, are in retreat across the Amundsen Sea Embayment (Rignot et al., 2026). Because WAIS is grounded largely below sea level, it is vulnerable to the Marine Ice Sheet Instability (MISI). This is a feedback mechanism whereby a retreating grounding line on a bed deepening inland exposes thicker ice to the ocean at the grounding line, leading to

© 2026 The Author(s). Journal of Geophysical Research: Earth Surface published by Wiley Periodicals LLC on behalf of American Geophysical Union. This is an open access article under the terms of the Creative Commons Attribution License, which permits use, distribution and reproduction in any medium, provided the original work is properly cited.

21699011, 2026, 12, Downloaded from https://agupubs.onlinelibrary.wiley.com/doi/10.1029/2026JF009300 by British Antarctic Survey, Wiley Online Library on [27/11/2026]. See the Terms and Conditions (https://onlinelibrary.wiley.com/terms-and-conditions) on Wiley Online Library for rules of use; OA articles are governed by the applicable Creative Commons License

increased ice flux over the grounding line. The result is unstable grounding line retreat, increased drawdown of inland ice, and ice loss irreversible on human timescales (Benn & Sugden, 2020; Mercer, 1978).

Thwaites Glacier, located in the Amundsen Sea region, is the second largest contributor to Antarctica's ice loss after the neighboring Pine Island Glacier (Mouginot et al., 2014; Otosaka et al., 2023; Rignot et al., 2019). Thwaites Glacier drains an area of 193 $\times$ 10^6 km^2, and in the period 1979–2017, contributed 1.8 mm of sea level rise out of WAIS' total 6.9 $\pm$ 0.6 mm (Rignot et al., 2019). In the period 1996–2025, the grounding line of Thwaites Glacier retreated 26 km, with the glacier losing 1161 $\pm$ 62 km^2 of grounded ice (Rignot et al., 2026). Unstable grounding line retreat consistent with MISI may already be underway at Thwaites and Pine Island Glaciers (Favier et al., 2014; Joughin et al., 2014). Over the past decade, the glaciological community's understanding of Thwaites Glacier's behavior has dramatically improved thanks to international research efforts such as the International Thwaites Glacier Collaboration (Scambos et al., 2017). However, knowledge gaps remain regarding the physical setting of Thwaites Glacier and key boundary conditions controlling flow, such as bed conditions and the factors controlling shear margin location (MacGregor et al., 2013).

Coupled ice-ocean models indicate that the retreat of the Thwaites Glacier grounding line is likely to be sporadic and controlled by transient pinning points developing at basal topographic highs, with dynamic stability depending both on melting around the pinning points (Bett et al., 2024) and the basal properties upstream (Parizek et al., 2013). One such potential pinning point is Ghost Ridge, a subglacial ridge ~65 km upstream of the present-day grounding line. As the grounding line retreats inland, Ghost Ridge may become increasingly important for Thwaites' stability (Schwans et al., 2023). Loss of ice shelf buttressing (Gudmundsson et al., 2023; Wild et al., 2022) and weak topographic control at the shear margins (MacGregor et al., 2013) mean that understanding the material properties of Thwaites' bed is critical for constraining model projections of the entire WAIS.

Glacier slip is represented in numerical models by sliding laws. Sliding laws relate basal shear stress to sliding velocity, aiming to describe the processes at the glacier sole that provide drag (see e.g. Alley et al., 2022; Brondex et al., 2017; Hank et al., 2026). The parameterization of slip remains a major source of uncertainty in sea level rise projections because using different sliding laws results in differences in ice sheet model outputs (e.g., Ritz et al., 2015). Numerous studies have demonstrated this for Pine Island and Thwaites Glaciers (e.g., Brondex et al., 2019; Joughin et al., 2019; Schwans et al., 2023; Yu et al., 2018). Sliding laws can be broadly divided into two types: "hard bed" and "soft bed", the former representing sliding over a rigid bed with ice deforming and regelating around obstacles, and the latter representing sliding primarily by deformation of subglacial till. Hard bed sliding is often described by a power law in which the basal shear stress depends on sliding velocity (Weertman, 1957), and can include a dependence on effective pressure—the difference between ice overburden and subglacial water pressure (Budd et al., 1979). Hard and soft beds may both be approximated by power laws, with viscous and plastic regimes represented by different exponents (e.g., Kazmierczak et al., 2022; Schwans et al., 2023). Alternatively, soft beds may be described by a Coulomb-type relation with basal shear stress dependent on till friction angle and effective pressure, but independent of sliding velocity (Tulaczyk et al., 2000). Some sliding laws depend on both sliding velocity and effective pressure (Schoof, 2005; Tsai et al., 2015; Zoet & Iverson, 2020). The physically based regularized Coulomb sliding law can capture both the rate strengthening and the Coulomb nature of glacial slip (Hansen, Zoet, & Muto, 2024; Hansen, Warburton, et al., 2024; Helanow et al., 2021; Zoet & Iverson, 2020) and has a strong dependence on the subglacial effective pressure. Changes in water pressure at the bed vary the effective pressure, weakening or strengthening till and impacting these forms of sliding law. Field observations of basal conditions are therefore important for the accurate representation of these physics in models.

Sampling the glacier bed directly by drilling boreholes is logistically difficult, expensive, time consuming and can deliver only point measurements across hundreds of square kilometers of an ice stream. Seismic surveys offer a means to map the distribution of hard and soft beds without drilling. The acoustic impedance Z_b of the glacier bed may be estimated from the normal-incidence seismic reflectivity, R_0, which is sensitive to the contrast in acoustic impedance across a reflecting interface, and has been used across West Antarctica (e.g., Rutford Ice Stream, Pine Island Glacier and Thwaites Glacier) to infer the distribution of hard and soft bed conditions (Brisbourne et al., 2017; Muto, Anandakrishnan, et al., 2019; Smith, 1997). Hard beds of consolidated or lithified sediment have higher acoustic impedances than those composed of unconsolidated sediment or actively deforming (dilatant) till. When wide-angle (incidence angle $\theta > 10°$) data have been acquired, this can be extended to amplitude-versus-angle analysis (AVA), which accounts for the angular dependence of the reflectivity of the ice-

21699011, 2026, 12, Downloaded from https://agupubs.onlinelibrary.wiley.com/doi/10.1029/2026JF009300 by British Antarctic Survey, Wiley Online Library on [27/11/2026]. See the Terms and Conditions (https://onlinelibrary.wiley.com/terms-and-conditions) on Wiley Online Library for rules of use; OA articles are governed by the applicable Creative Commons License

bed interface, $R(\theta)$. AVA is sensitive to contrasts in a wider range of properties than normal-incidence surveys: $R(\theta)$ depends on contrasts in compressional-wave velocity v_p, shear-wave velocity v_s, and density ρ across the reflecting interface, whereas R_0 depends only on contrasts in v_p and ρ. AVA results are often framed in terms of two quantities: acoustic impedance Z and Poisson's ratio ν. This can aid interpretation (Agnew et al., 2025; Booth et al., 2012; Shuey, 1985). Due to its greater sensitivity to the properties of the bed under shear stresses, which ultimately determine the sliding law, AVA analysis has the potential to provide greater insight into ice-bed interface processes and the links between seismic field studies and laboratory studies of glacial slip (e.g., Hansen, Zoet, & Muto, 2024; Hansen, Warburton, et al., 2024; Zoet & Iverson, 2020).

Despite decades of surveys of basal seismic reflectivity in Antarctica, translating these results into improvements in ice-sheet models remains elusive (e.g., Kyrke-Smith et al., 2017). While acoustic impedance may be used to distinguish between hard and soft beds, determining the appropriate sliding law is difficult, and key parameters such as effective pressure remain unconstrained in most cases. Recent work by Hank et al. (2026) provides a framework for using basal acoustic impedance data to constrain ice sheet models using viscous grain shearing theory (VGS, Buckingham, 1997; Buckingham, 2005, 2007), a mathematical framework originally developed for marine sediments that relates the seismic properties of a saturated, unconsolidated sediment to the elastic properties of the constituent mineral and pore fluid, mineral grain size, porosity, effective pressure and seismic frequency. In this paper, we combine seismic AVA analysis with VGS theory to provide constraints on the porosity and effective pressure at the glacier bed. The aim is to close the gap between seismic measurements and useful inputs for ice sheet models. Constraints on the properties of bedforms beneath an active ice stream will also aid understanding of the conditions under which these features form, eventually aiding paleo-ice sheet reconstructions from observations of landforms in present-day deglaciated landscapes.

Unusually for an Antarctic ice stream, Thwaites Glacier flows across, rather than along, the underlying rift system, with a series of roughly flow-perpendicular ridges and highlands interspersed with sedimentary basins between them (Jordan et al., 2023). Previous seismic surveys (Clyne et al., 2020; Muto, Anandakrishnan, et al., 2019) at two subglacial ridges upstream of Ghost Ridge revealed a highly heterogeneous bed, with differences in bed properties between the stoss and lee sides of subglacial bedforms, analogous to examples in present-day deglaciated areas (e.g., Evans & Hansom, 1996; Muto, Alley et al., 2019). Recent geophysical work has included seismic refraction and gravimetric surveys (Borthwick et al., 2025), which revealed a sedimentary basin underlain by mafic intrusions, and an extensive survey using a vibroseismic system (Zeising et al., 2026). The latter survey includes an across-flow survey from a central flowline to the Eastern shear margin, and observed similar bed variability, with harder material on the stoss and softer material on the lee sides of bedforms. Figure 1 shows the locations of our survey and these previous studies, along with an approximately along-flow profile of surface and bed topography upstream and downstream of our survey location taken from Bedmap3 (Pritchard et al., 2025). The observed heterogeneity in bed properties is likely to have ice dynamic impacts; modelling has shown that sliding over mixed bed types can produce retreat rates outside the end members observed for uniform hard or soft beds (Koellner et al., 2019; Schwans et al., 2026).

Previous studies have inferred the presence of soft subglacial till from the ice-bed seismic reflectivity and interpreted that the till is dilated (e.g., Anandakrishnan, 2003; Brisbourne et al., 2017; Smith, 1997). However, motion of glaciers over soft till beds has also been observed where the ice is decoupled from the bed and most of the motion is accounted for by the sliding of ice over till (Engelhardt & Kamb, 1998; Iverson et al., 1995). Despite a well-founded association between soft subglacial tills and active deformation supported by drilling and in situ observations (e.g., Boulton, 1979; Iverson et al., 1994; Kamb, 2001; Truffer et al., 2000), when basal effective pressures are extremely low these materials may not be undergoing pervasive deformation. Throughout our paper we make a distinction between the terms "soft till" and "dilatant till", using the former in the context of identifying a subglacial material based on seismic results, and using "dilatant till" only when making a judgment about whether the till is actively deforming.

In this study we determine bed properties in the region immediately upstream of Ghost Ridge. We first show a processed seismic section and estimate bed acoustic impedance Z_b from normal-incidence seismic reflectivity. We then use amplitude-versus-angle (AVA) analysis to further constrain the properties of the basal material. We use a novel combination of AVA data and viscous grain shearing theory (Buckingham, 1997, 2005, 2007) to estimate sediment porosity and infer a difference in effective pressure between nearby sections of bed with different characters.

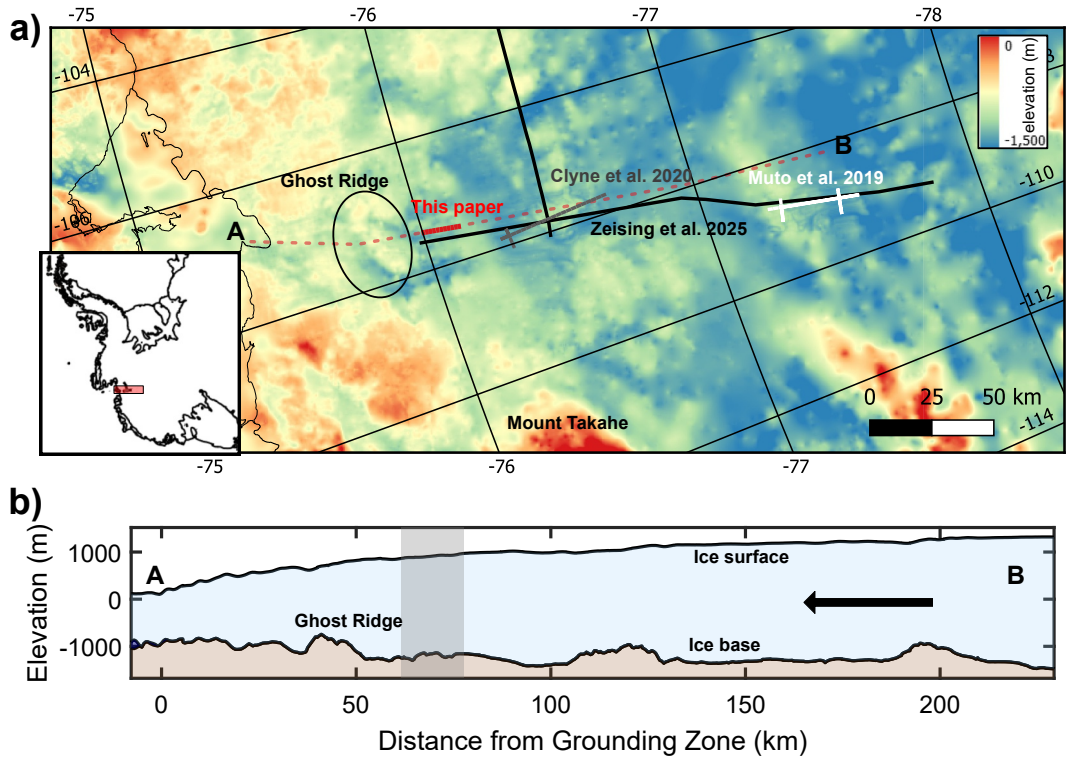

Figure 1. (a) Map showing the location of this survey in the context of previous studies on Thwaites Glacier reporting basal properties: Muto, Anandakrishnan, et al. (2019), Clyne et al. (2020), and part of the survey reported by Zeising et al. (2026). Ghost Ridge is shown in the black ellipse, roughly 65 km upstream of the grounding line (black solid line). Color scale shows bed elevation from Bedmap3 (Pritchard et al., 2025). Inset shows location within West Antarctica. (b) Profile of ice surface and bed elevation along the approximate flowline AB, showing the location of Ghost ridge and the area in the present study (shaded area). Ice flow is from B to A, in the direction of the arrow. Bed and surface elevation from Bedmap3.

2. Data Acquisition

During January 2024, a 14.4 km long seismic profile was acquired upstream of Ghost Ridge, Thwaites Glacier. The location of the survey is marked on Figure 1, along with the locations of previous reflection seismic surveys from which basal acoustic impedance has been estimated (Clyne et al., 2020; Muto, Anandakrishnan, et al., 2019; Zeising et al., 2026). The survey described in this work lies at the downstream limit of the sedimentary basin described by Borthwick et al. (2025). Georods, a type of four-element geophone in which the receiver elements are wired in series to improve the signal-to-noise (Voigt et al., 2013), were used to acquire the data. Each spread consisted of 96 40 Hz georods buried ∼30 cm below the snow surface at 20 m intervals (total spread length 1,920 m). Sources were initiated at 20 m, 1,940 m and 3,860 m offset upstream of the first receiver. The spread was then moved 960 m upstream. Sources were initiated in hot-water-drilled holes at between 2 and 52 m depth (median 36 m), backfilled with snow and left to sinter for at least 24 hr. Charges for most 20 m offset shots were 450 g of Pentolite, except for one 150 g charge that was loaded due to insufficient shothole depth for a larger charge, and one larger 14 kg charge initiated as part of a separate refraction survey (Borthwick et al., 2025). 1,940 m (mid-offset) and 3,860 m (far-offset) offset shots used 600 g Pentolite charges. The ice surface elevation varies from 851 m at the downstream end of the profile to 930 m at the upstream end. The dominant frequency of the wavelet is 200 Hz and the first Fresnel radius is 140 m for 2 km thick ice. Wide-angle data were acquired continuously along the seismic profile, with maximum source-receiver offsets of 5,780 m.

3. Methods

In this study, we use normal-incidence techniques along the entire seismic profile and AVA analysis in localized areas where data are suitable. Where the ice-bed interface is sufficiently flat and homogeneous to permit AVA analysis, traces were grouped into 6 supergathers such that the basal reflection wavelet was consistent in each

21699011, 2026, 12, Downloaded from https://agupubs.onlinelibrary.wiley.com/doi/10.1029/2026JF009300 by British Antarctic Survey, Wiley Online Library on [27/11/2026]. See the Terms and Conditions (https://onlinelibrary.wiley.com/terms-and-conditions) on Wiley Online Library for rules of use; OA articles are governed by the applicable Creative Commons License

21699011, 2026, 12, Downloaded from https://agupubs.onlinelibrary.wiley.com/doi/10.1029/2026JF009300 by British Antarctic Survey, Wiley Online Library on [27/11/2026]. See the Terms and Conditions (https://onlinelibrary.wiley.com/terms-and-conditions) on Wiley Online Library for rules of use; OA articles are governed by the applicable Creative Commons License

Table 1
AVA Reflection Points (Distances From the Downstream End of the Seismic Line)

AVA supergather	Reflection point x location range (m)
AVA01	3,840–4,790
AVA02	5,080–5,750
AVA03	7,680–8,500
AVA04	8,640–9,160
AVA05	10,560–11,510
AVA06	11,520–12,470

supergather. These supergathers span a range of reflection points from 3.84 to 12.47 km along the profile and are numbered "AVA01" to "AVA06" (see Table 1 for reflection point locations). An example of an AVA supergather (AVA03) is shown in Figure 2, with direct waves, the basal reflection and its source ghost marked. Wavelets of direct waves and basal reflections at near and far offsets are inset. At this location, the basal reflection has a negative polarity at normal incidence and a positive polarity at large angles, reversing at 2,200 m offset. Polarity reversals such as these are diagnostic of subglacial material properties (Anandakrishnan, 2003).

The amplitude A of a wavelet returned from an interface with reflectivity R along a ray path of length r is:

$$A(\theta) = A_0 R(\theta)\gamma(r,\theta)e^{-\alpha(f)r}, \tag{1}$$

where $\alpha(f) = \pi f/Qv$ is the attenuation coefficient for a wavelet of frequency f and velocity v. Q is the seismic quality factor, which is inversely proportional to the fractional energy loss per wave cycle. γ is the geometric spreading factor. To obtain $R(\theta)$, Equation 1 is rearranged to

$$R(\theta) = \frac{A(\theta)}{A_0}\frac{1}{\gamma(\theta)}e^{\alpha r}. \tag{2}$$

The basal acoustic impedance is estimated using R_0:

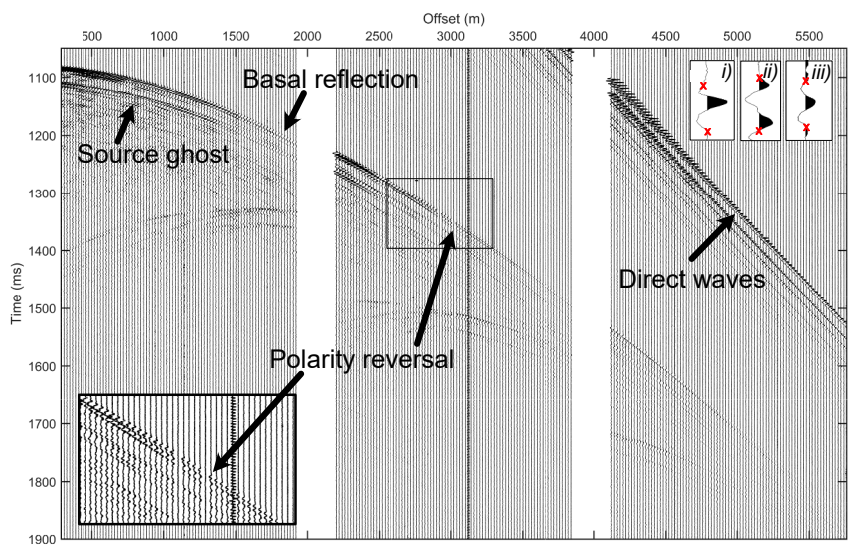

Figure 2. Traces from AVA supergather AVA03, with basal reflection, source ghost and direct waves marked. Top right insets show wavelets and picks (red crosses) for: (i) direct arrival (source wavelet); (ii) basal reflection at 1,580 m offset; (iii) basal reflection at 5,180 m offset. Bottom left inset shows detail of wavelet polarity reversal at 2,200 m offset.

$$Z_{\text{bed}} = Z_{\text{ice}} \frac{1 + R_0}{1 - R_0}, \tag{3}$$

where Z_{ice} is the acoustic impedance in the ice and Z_{bed} is the acoustic impedance in the bed. Basal reflections were picked at the second zero crossing either side of the wavelet maximum (Figure 2, top right inset), with the root-mean-square of this wavelet giving the amplitude A.

Seismic data processing followed two separate workflows: (a) to obtain a time section of the subsurface from the near-offset data and (b) to obtain absolute reflection amplitudes to estimate the basal acoustic impedance and perform amplitude-versus-angle analysis. Workflow (a) consisted of making static corrections to account for shot depth, balancing trace amplitudes, normal moveout corrections at a velocity of 3,750 m/s, removal of the source ghost with predictive deconvolution, bandpass filtering and Kirchhoff time migration. Workflow (b) applied geometric, attenuation and source amplitude corrections to wavelet amplitudes to obtain the reflection coefficient $R(\theta)$. Bed acoustic impedance Z_b was then estimated from the normal-incidence traces (source-receiver offset $<$700 m, incidence angle $<10°$) using Equation 3, and AVA inversion was performed on suitable wide-angle data. The following sections provide more details about the corrections applied to recover $R(\theta)$.

3.1. Recovery of $R(\theta)$

3.1.1. Velocity Model, Raytracing, Geometric Correction and Attenuation

A depth-dependent velocity model is needed for calculating geometric corrections when the source is buried. Near surface velocities were taken from short refraction surveys at similar elevations on Pine Island Glacier (PIG), where accumulation is assumed to be similar (Arthern et al., 2006). The mean of six profiles at elevations varying from 700 to 900 m (Brisbourne et al., 2017) was taken and the result used to obtain geometric corrections by raytracing. The velocity was assumed constant at $V_{\text{ice}} = 3{,}780$ m s^{-1} from the base of the firn to the bed, taken from the maximum velocity of the mean PIG velocity profile. Amplitudes were corrected for the incidence angle at the receiver θ_r such that the true amplitude $A_{\text{true}} = A_v / \cos\theta_r$, where A_v is the amplitude recorded on the vertical component georods. θ_r were obtained through raytracing. We use a form of the geometric correction $\gamma(r)$ that accounts for not only spherical spreading along the ray path r but also the difference in burial depth between source and receiver and the velocity gradient in the medium (Medwin & Clay, 1998, Equation 3.3.31). Reflection points were taken as the source-receiver midpoint. Over the first Fresnel zone, dip angles are $<11°$, so the bed was assumed flat for AVA analysis (Muerdter et al., 2005).

Attenuation in the ice column was estimated by the spectral ratio method, using available primary and first long-path multiple reflections (Båth, 1974; Dasgupta & Clark, 1998; Teng, 1968). Primary and first long-path multiple wavelets at near normal-incidence from shot ID 749 (CMP x-coordinates 4,450–4,780 m) were stacked prior to spectral ratio estimation. The quality factor, Q, was measured as $Q = 445 \pm 30$, giving $\alpha = (3.7 \pm 0.3) \times 10^{-4}$ m^{-1} at $f = 200$ Hz. This correction was applied to path lengths r obtained from raytracing through the velocity model from PIG.

3.1.2. Source Amplitude Correction

Estimation of the source amplitude, A_0, is a key source of uncertainty in glacial seismic reflectivity studies (Horgan et al., 2021; Smith, 2007). To estimate A_0 and correct for differences in A_0 between shots, an approach was used combining amplitudes of primary reflections, first long-path multiples and direct waves. At normal incidence, A_0 may be estimated from the amplitudes of the primary reflection, A_1, and its first long-path multiple, A_2:

$$A_0 = \frac{{A_1}^2}{A_2} \frac{1}{2\gamma_1}, \tag{4}$$

where γ_1 is the geometric spreading factor for the primary reflection (Holland & Anandakrishnan, 2009). This method of estimating A_0 is more robust than others which estimate A_0 from direct waves and is therefore preferred where long-path multiples are present with a sufficient signal-to-noise ratio (Horgan et al., 2021). However, long-path multiples were not recorded along most of our seismic line, similarly to other data sets acquired on Thwaites Glacier (Clyne et al., 2020; Muto, Anandakrishnan, et al., 2019). Consequently, Equation 4 was used to estimate

21699011, 2026, 12, Downloaded from https://agupubs.onlinelibrary.wiley.com/doi/10.1029/2026JF009300 by British Antarctic Survey, Wiley Online Library on [27/11/2026]. See the Terms and Conditions (https://onlinelibrary.wiley.com/terms-and-conditions) on Wiley Online Library for rules of use; OA articles are governed by the applicable Creative Commons License

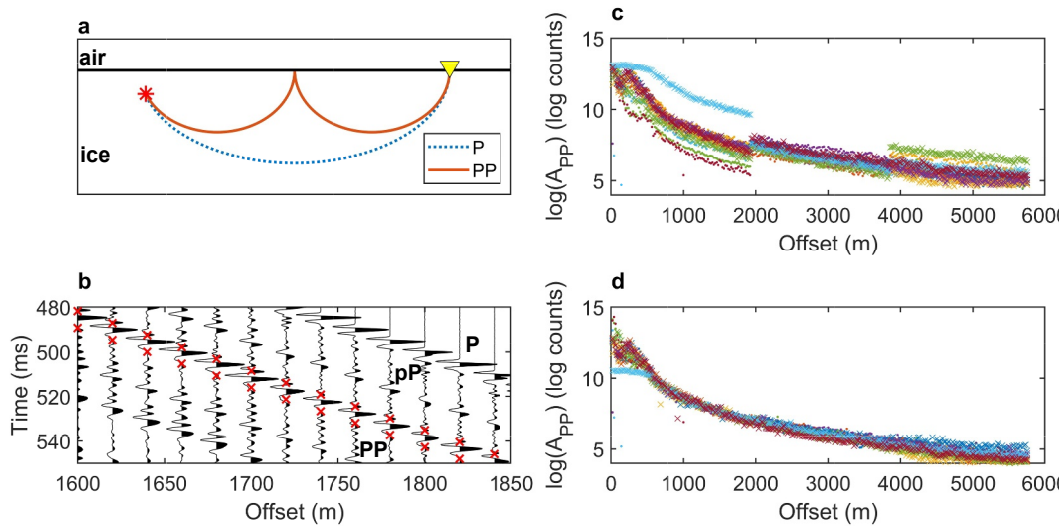

Figure 3. Panel (a) ray paths of direct P and PP waves. Red star shows shot location and the yellow triangle shows receiver location. Horizontal line is the glacier surface. Panel (b) sample of direct waves recorded on shot 749. First arrivals are P, followed by source ghost pP and the phase of interest, PP. Panel (c) raw PP amplitudes and (d) corrected PP amplitudes. The same correction is applied to amplitude returns from the bed. Three shots were recorded with each georod spread; points are colored the same for a single georod spread.

absolute A_0 where a multiple was recorded (shot ID 749 at location x = 4,800 m). Scalar corrections were computed to apply to each other shot based on direct wave amplitudes. Far-offset (>4 km) first arrivals displayed amplitudes deviating from the expected exponential decay; we were unable to determine the cause of this effect but hypothesize that it is a result of constructive interference in the firn column preserving the apparent amplitude of the direct wave at far offsets. The direct wave reflected once at the ice surface, PP, did not show this behavior at the relevant offsets, so PP amplitudes were used for the source amplitude correction, assuming a reflectivity of −1 at the snow-air interface (Figure 3b). The corrections were then computed in two stages. Amplitudes from each 20 m offset shot were multiplied by a scalar chosen to minimize the misfit of the corrected logarithmic amplitudes to the PP direct wave recorded from shot 749. Next, amplitudes of mid- and far-offset shots recorded by each single georod spread were corrected to ensure continuity of the PP direct wave logarithmic amplitudes between near-, mid-, and far-offset shots (Figures 3c and 3d). Note that this normalizes the amplitudes to the first shot in each spread. In this manner A_0 corrections were estimated for each shot gather before sorting traces into supergathers for AVA analysis.

3.1.3. Basal Ice Properties

When estimating bed acoustic impedance from Equation 3 or performing an AVA inversion, the elastic properties of the basal ice must be assumed. With a few exceptions (e.g., Chandra et al., 2025; Horgan et al., 2021) the basal ice is generally assumed to be free of sediment for seismic reflectivity studies. However, the glacier sole entrains debris by regelation, freeze on, shearing and mixing (e.g., Alley et al., 1997; Kirkbride, 2002). Debris-rich basal ice can be meters thick and contain up to 40% debris by volume (Kirkbride, 2002); in extreme cases debris-laden ice packages hundreds of meters thick have been inferred from radar data (Franke et al., 2024). Borehole imagery of basal ice at Kamb ice stream (Christoffersen et al., 2010; Engelhardt & Kamb, 2013) revealed basal debris in concentrations of 20% in a sequence 8 m thick, which Christoffersen et al. (2010) interpreted as a result of enhanced debris entrainment during ice stream stagnation episodes. These concentrations may be higher than representative for the fast-flowing Thwaites Glacier. However, hot water drilling on the fast-flowing Rutford Ice Stream also found sediment in the basal ice (Smith et al., 2021). Images of basal ice taken immediately downstream of the Thwaites Glacier grounding zone by an underwater vehicle show debris-laden ice, indicating that basal debris entrainment persists to the Thwaites grounding zone (Schmidt et al., 2023). We assume that 10% debris by volume is present in the basal ice of Thwaites Glacier over a seismic wavelength (∼20 m for a 200 Hz wavelet).

21699011, 2026, 12, Downloaded from https://agupubs.onlinelibrary.wiley.com/doi/10.1029/2026JF009300 by British Antarctic Survey, Wiley Online Library on [27/11/2026]. See the Terms and Conditions (https://onlinelibrary.wiley.com/terms-and-conditions) on Wiley Online Library for rules of use; OA articles are governed by the applicable Creative Commons License

21699011, 2026, 12, Downloaded from https://agupubs.onlinelibrary.wiley.com/doi/10.1029/2026JF009300 by British Antarctic Survey, Wiley Online Library on [27/11/2026]. See the Terms and Conditions (https://onlinelibrary.wiley.com/terms-and-conditions) on Wiley Online Library for rules of use; OA articles are governed by the applicable Creative Commons License

Table 2
Properties of Clean and Debris-Laden Basal Ice Assumed for Estimation of Acoustic Impedance Z_b From Normal-Incidence Data and for AVA Inversion

Material	v_p (m s^{-1})	v_s (m s^{-1})	Density (kg m^{-3})	Z ($\times 10^6$ kg m^{-2} s^{-1})
Ice (clean)[a]	3,800	1,840	917	3.45
Ice (10% debris, this study[b])	3,760	1,910	1,090	4.10
Quartz[c]	6,040	4,120	2,650	16.0

[a]Taken from Peters et al. (2006). [b]Estimated from a Bruggeman mixing model (Bruggeman, 1937; Röthlisberger, 1972). [c]Taken from Mavko al. (2009).

To account for the ambiguity arising from this assumption, we present two sets of results: (a) results arising from an assumption of clean basal ice, to facilitate comparison with earlier studies and qualitatively interpret the bed character (Brisbourne et al., 2017; Christianson et al., 2014; Luthra et al., 2016; Muto, Anandakrishnan, et al., 2019; Peters et al., 2007), and (b) results arising from an assumption of debris-laden basal ice, to give our best estimate of bed properties. We compute the likely properties of debris-laden ice using a Bruggeman mixing model (Bruggeman, 1937), after Röthlisberger (1972) and Horgan et al. (2021), assuming 10% by volume debris inclusions composed of quartz. These properties are similar to those estimated by Horgan et al. (2021) by AVA analysis at the grounding zone of Whillans Ice Stream for an estimated 7% debris content. The relevant properties of clean and debris-laden basal ice are given in Table 2.

3.2. AVA Inversion

After $R(\theta)$ had been estimated using the corrections described above, AVA inversion followed a Bayesian Markov-Chain-Monte-Carlo approach (Agnew et al., 2025) using the Metropolis-Hastings algorithm (Hastings, 1970; Metropolis et al., 1953) with forward modelling using the exact Knott-Zoeppritz equations (Knott, 1899; Zoeppritz, 1919). This method estimates ρ, v_p and v_s from their posterior distributions, given prior assumptions and AVA data, using Bayes' rule. To stabilize the inversion, amplitudes and errors were averaged into 2° bins. We use a Gaussian likelihood weighted by the error on each value of $R(\theta)$, so uncertainties in the corrections applied are propagated through the inversion. In glaciological AVA inversions, results drawn from marginal distributions of acoustic impedance Z and Poisson's ratio ν are generally more accurate and better constrained than those presented in terms of ρ, v_p and v_s (Agnew et al., 2025). After posterior distributions of ρ, v_p v_s were obtained, marginal distributions of acoustic impedance Z, Poisson's ratio ν, shear modulus μ, and bulk modulus κ were computed, using:

$$Z = \rho v_p, \tag{5}$$

$$\nu = \frac{v_p^2 - 2v_s^2}{2\left(v_p^2 - v_s^2\right)}, \tag{6}$$

$$\mu = \rho v_s^2, \tag{7}$$

$$\kappa = \rho\left(v_p^2 - \frac{4}{3}v_s^2\right). \tag{8}$$

Results given are medians ± half interquartile ranges from the marginal distributions. We set uniform priors for v_p, v_s, and ρ in the subglacial material, following those set by Zechmann et al. (2018) and Horgan et al. (2021)

Table 3
Prior Assumptions of Bed Properties, After Zechmann et al. (2018), Horgan et al. (2021)

v_p (m s^{-1})	1,440–2,300
v_s (m s^{-1})	0–1,150
ρ (kg m^{-3})	1,000–2,500

Note. We assume uniform probabilities within these bounds.

21699011, 2026, 12, Downloaded from https://agupubs.onlinelibrary.wiley.com/doi/10.1029/2026JF009300 by British Antarctic Survey, Wiley Online Library on [27/11/2026]. See the Terms and Conditions (https://onlinelibrary.wiley.com/terms-and-conditions) on Wiley Online Library for rules of use; OA articles are governed by the applicable Creative Commons License

(Table 3). The velocities and density of the basal ice are allowed by the inversion to vary with a standard deviation of $\delta v_{p,\mathrm{ice}} = \delta v_{s,\mathrm{ice}} = 50$ m s^{-1} and $\delta \rho_{\mathrm{ice}} = 50$ kg m^{-3}.

3.3. Viscous Grain Shearing

VGS theory relates the seismic compressional and shear wave velocities of an unconsolidated sediment to the elastic properties of the constituent mineral and pore fluid, mineral grain size d, porosity ϕ, effective pressure N and frequency f. We use VGS here to constrain the ranges of effective pressure, grain size and porosity consistent with our AVA inversion results, using a workflow we refer to as AVA-VGS. This workflow takes the outputs of an AVA inversion, $Z \pm \delta Z$ and $\nu \pm \delta \nu$, and selects combinations of N, ϕ and d which predict acoustic impedances and Poisson's ratios within the uncertainties of the AVA inversion results. We use $f = 200$ Hz from the dominant frequency of the basal reflection, and assume the sediment is composed of quartz. All other parameters used in VGS are the same as in Hank et al. (2026). The governing equations and a list of parameters used are given in Appendix A.

We performed a 3D grid search of N, ϕ and d covering the ranges: $0 \leq N \leq 5{,}000$ kPa (increment $\Delta N = 20$ kPa); $0.35 \leq \phi \leq 0.65$ (increment $\delta d = 0.002$); and 0.001 mm $\leq d \leq$ 1 mm. The increment for d was logarithmic and determined from the quantity ψ such that $d = 2^{\psi} \times 10^{-3}$ mm, and $0 \leq \psi \leq 10$ with an increment of $\Delta \psi = 0.02$. This grid search resulted in 19×10^6 combinations. For all combinations, acoustic impedance and Poisson's ratio were predicted from VGS. These predictions were then sieved for the two regions at (a) AVA03/04 and (b) AVA05/06, chosen to represent two areas of contrasting bed character from the normal-incidence and AVA data. For each region, the limits of the uncertainties on the two AVA results were combined to give maximum and minimum limits on Z and ν for the sieving. Any prediction falling outside of these limits for the regions (a) AVA03/04 and (b) AVA05/06 was excluded.

Effective pressure and grain size are multiplied together in VGS, meaning that their constraint is nonunique. Consequently, we give results for their product, dN. Note that these ranges tell us only what is consistent with the VGS theory and contain no prior information other than the choice of grid. The searched porosity range is set deliberately wide to avoid truncating the result distributions. This is intended to illustrate the constraints VGS can provide. We consider $\phi > 0.6$ implausible for these sites: by borehole access, Kamb (2001) showed maximum matrix porosities of 0.6 which decreased rapidly with depth to $\phi < 0.5$.

4. Results

4.1. Normal-Incidence Data: Bedforms and Spatial Variation of Z

Figure 4a shows the migrated time section for our survey. Note that weathering and surface elevation corrections have not been applied, so Figure 4a represents the ice thickness rather than bed elevation. Figure 4b shows the basal reflection coefficient for normal-incidence traces, and Figure 4c shows the estimated acoustic impedance of the bed for both scenarios of clean basal ice (black dots, $Z_{\mathrm{ice}} = 3.45 \times 10^6$ kg m^{-2} s^{-1}) and debris-laden basal ice (blue crosses, $Z_{\mathrm{ice}} = 4.10 \times 10^6$ kg m^{-2} s^{-1}). The shaded areas represent acoustic impedance interpreted by previous authors as consistent with dilatant till (yellow shading) and unconsolidated stiff or consolidated sediments (gray shading) (Atre & Bentley, 1993; Christianson et al., 2014). Zeising et al. (2026) divide these properties into 3 categories based on an interpretation of the likely dominant mechanism of basal motion: (a) motion dominated by till deformation when $Z < 2.72 \times 10^6$ kg m^{-2} s^{-1}, (b) motion dominated by basal sliding when $Z > 3.24 \times 10^6$ kg m^{-2} s^{-1}. Between these limits Zeising et al. (2026) interpret an "ambiguous bed", where the acoustic impedance ranges of dilatant sediments and unconsolidated stiff sediments overlap. Interpreting a sliding mechanism from acoustic impedance in this range is not possible because of the nonuniqueness of Z_b. These ranges were partly derived from seismic studies that assumed clean basal ice (Peters et al., 2006, 2007), so we make qualitative interpretations of the bed type based on these ranges and our clean-ice derived results. Acoustic impedance values quoted in the text result from our debris-laden ice assumption and represent our best estimate of subglacial properties.

Over our 14.4 km long profile, bed acoustic impedance indicates the presence of subglacial sediments; nowhere do we find acoustic impedances consistent with strongly lithified sediments or crystalline basement. We do not observe a clear reflection from the base of the sediment layer so are unable to constrain its thickness. We observe a variety of bedforms and alternating stiff and soft beds, with variation between soft sediment areas and stiff or

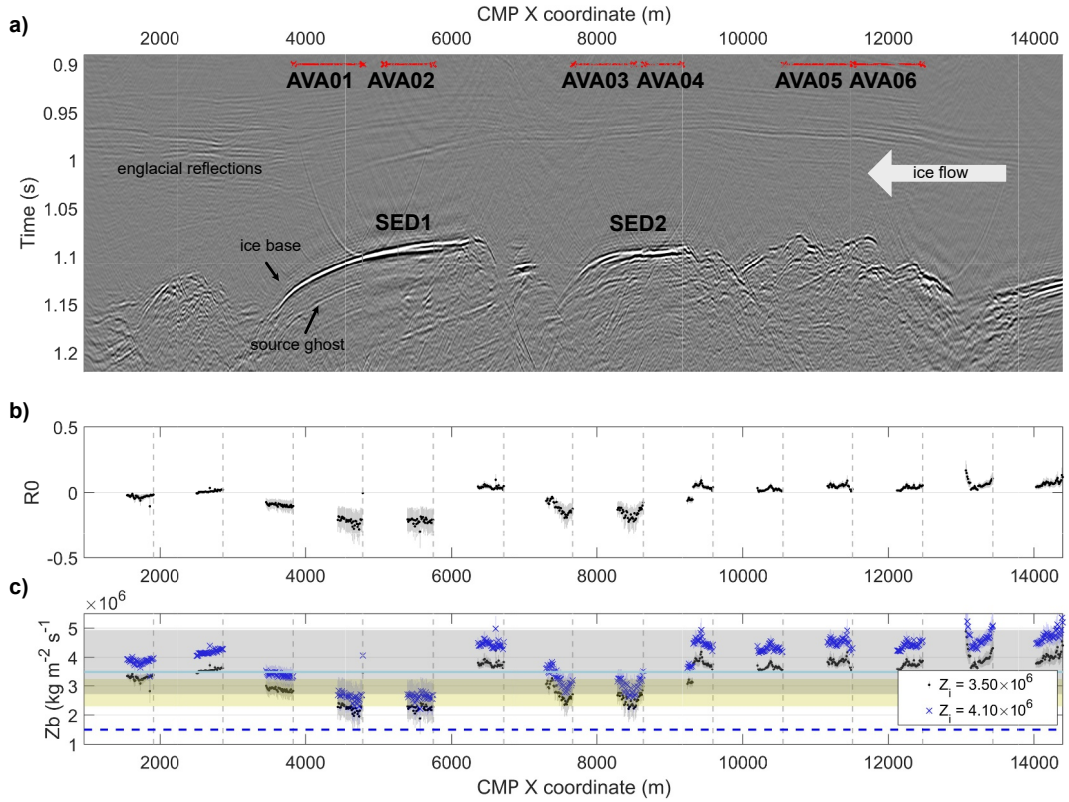

Figure 4. (a) Migrated time section, from 20 m offset shots. Location of AVA reflection points for AVA supergathers AVA01-AVA06 are marked with red horizontal lines. *y*-axis is two-way travel time. Ice flow is right to left. Residual source ghost energy is visible despite deghosting. (b) Normal-incidence reflection coefficient (R_0) processed from 20 m offset shots (traces for which $\theta < 10^{\circ}$ only are used). (c) Acoustic impedance of subglacial material. Blue dashed line marks acoustic impedance of water, yellow shaded box marks range of Z for dilatant till and gray shaded box marks range of Z for stiff till and consolidated sediments (Atre & Bentley, 1993; Christianson et al., 2014). Light blue solid line shows acoustic impedance of clean ice. Black points and error bars show bed acoustic impedance if ice is assumed to be clean $(Z_{\text{ice}} = 3.45 \times 10^6 \text{ kg m}^{-2} \text{ s}^{-2})$. Blue crosses and error bars show bed acoustic impedance if basal ice is assumed to be debris-laden $(Z_{\text{ice}} = 4.10 \times 10^6 \text{ kg m}^{-2} \text{ s}^{-2})$. Each data point in (b, c) comes from one trace.

consolidated sediments. Starting from Ghost Ridge at the downstream end of our line and moving upstream (from $x = 0$ km) we image a rough section of bed, possibly surrounded by sedimentary infill or moat-like features ($x \sim 3$ km). In this region the peak of the rougher feature ($x = 2.3$ km, positive polarity) is likely composed of stiffer and harder material than the surrounding low points, which appear as negative polarity reflectors. Between $x = 4$ km and $x = 6$ km, we image a prominent crag and tail feature with a height of approximately 130 m, which we refer to as SED1. The tail of this bedform is likely composed of soft sediments and shows a strong negative polarity reflection, with an acoustic impedance $<3 \times 10^6$ kg m^{-2} s^{-1}. The highest point on the bedform has the lowest acoustic impedance, with acoustic impedances increasing in the sediment downstream. The stoss side is stiffer, with a positive polarity reflection and acoustic impedance $\sim 4.4 \times 10^6$ kg m^{-2} s^{-1}. This is indicative of more consolidated material and/or higher effective pressures, but is too low to indicate exposed crystalline bedrock or strongly lithified sedimentary rock. This indicates that sediments are present even on the stoss side of the bedform.

Upstream from SED1 there is another smooth, negative polarity reflector which we call SED2, between $x = 7$ km and $x = 9$ km. SED2 does not show the steep relief of a crag and tail, instead emerging from more rolling topography upstream. At $x = 9.3$ km, there is a shift in character of the ice-bed return from negative polarity downstream to positive upstream; this may capture the transition between soft and hard bed regimes. Upstream of SED2, between $x = 10$ km and the end of our profile, the ice-bed contact is rougher and the bed has a higher acoustic impedance, indicating a greater level of consolidation, lower porosity and/or higher effective pressure.

21699011, 2026, 12, Downloaded from https://agupubs.onlinelibrary.wiley.com/doi/10.1029/2026JF009300 by British Antarctic Survey, Wiley Online Library on [27/11/2026]. See the Terms and Conditions (https://onlinelibrary.wiley.com/terms-and-conditions) on Wiley Online Library for rules of use; OA articles are governed by the applicable Creative Commons License

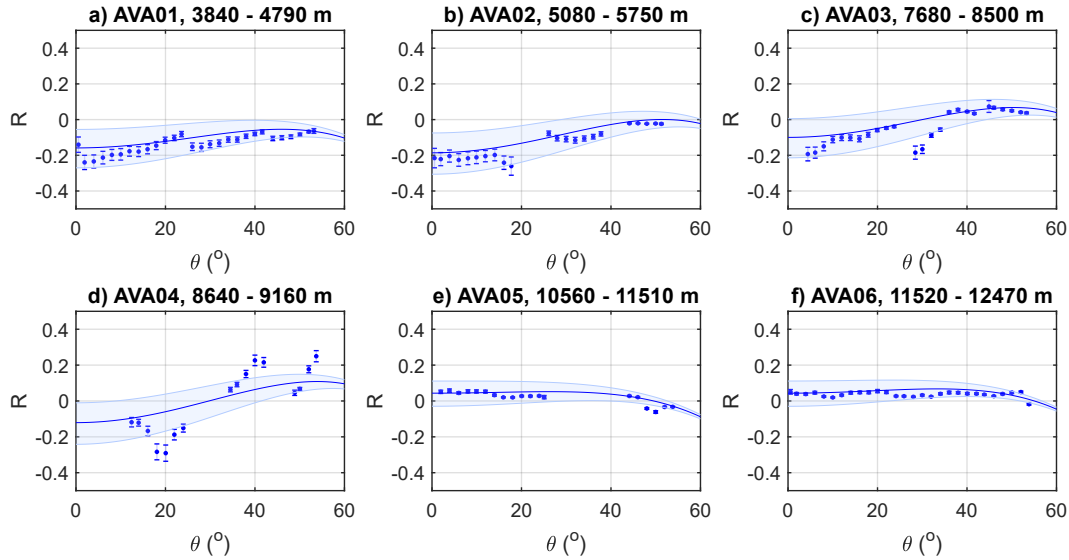

Figure 5. AVA responses recorded at six locations. Amplitudes of individual traces are averaged into 2-degree bins. Solid line plotted through the center of the data points is the AVA response resulting from the median properties of the posterior distributions, and shaded area shows the area between AVA curves resulting from the uncertainty bounds taken from the interquartile range of posterior distributions (Table 4). These are AVA curves resulting from basal properties in Table 4 underlying debris-laden basal ice.

We also image a series of englacial reflections ~200 m above the bed; we do not analyze these in detail but attribute them to a change in crystal orientation fabric in the lower portion of the ice column (Hofstede et al., 2013; Horgan et al., 2011).

4.2. AVA Results

The AVA results we present come from six supergathers across three distinct regions of bed character (locations: Table 1). These can be grouped into two supergathers per region: AVA01 and AVA02 are over the bedform SED1, AVA03 and AVA04 are over the bedform SED2, and AVA05 and AVA06 are over the rougher and stiffer section of bed between 10 and 12 km along the line. Figure 5 shows the six AVA responses (points and error bars). The lines show the predicted AVA response of the median model, and the shaded areas indicate the predicted AVA response of the median ± half interquartile range models. We attribute the apparent stepping in the AVA responses to the use of supergathers containing a spread of reflection points. AVA responses from the sedimentary features SED1 (a, b) and SED2 (c, d) show similar characters, with negative normal-incidence reflection coefficients and positive gradients with incidence angle at $\theta > 50°$. The reflection from SED2 (c, d, AVA03 and AVA04) reverses polarity from negative to positive at $\theta = 30°$ (supergather shown in Figure 2). Upstream, AVA05 and AVA06 show the opposite character, with weakly positive R_0, a relatively flat AVA gradient and polarities reversing from positive to negative at $\theta \sim 50°$.

To put our results for Z, ν and μ in the context of the glaciological AVA literature, we show results from previous AVA studies in Antarctica and Greenland (Christianson et al., 2014; Horgan et al., 2021; Luthra et al., 2016, 2017; Peters et al., 2007) alongside ours (Figure 6). As before, comparison of our results with other authors' results is most straightforward with the plotted black crosses (clean basal ice derived). Note the study by Horgan et al. (2021) used a debris-laden basal ice assumption. The softer materials at AVA02-04 display the highest Poisson's ratios and lowest shear moduli of all the sites. Bed shear modulus is higher at AVA01, and higher still at AVA05-06. Results of inversion for ρ, v_p, v_s, Z, ν, μ and K are given in Table 4. See Appendix B for results assuming clean basal ice (Table B1).

We interpret AVA responses at sites AVA02 to AVA04 as arising from subglacial soft till based on their low acoustic impedance, high Poisson's ratios and low shear moduli. These results lie in the ranges of results obtained by previous authors, all having $\nu > 0.45$ and $\mu < 0.5$ GPa. The till beneath site AVA01 and AVA02 is stiffer

21699011, 2026, 12, Downloaded from https://agupubs.onlinelibrary.wiley.com/doi/10.1029/2026JF009300 by British Antarctic Survey, Wiley Online Library on [27/11/2026]. See the Terms and Conditions (https://onlinelibrary.wiley.com/terms-and-conditions) on Wiley Online Library for rules of use; OA articles are governed by the applicable Creative Commons License

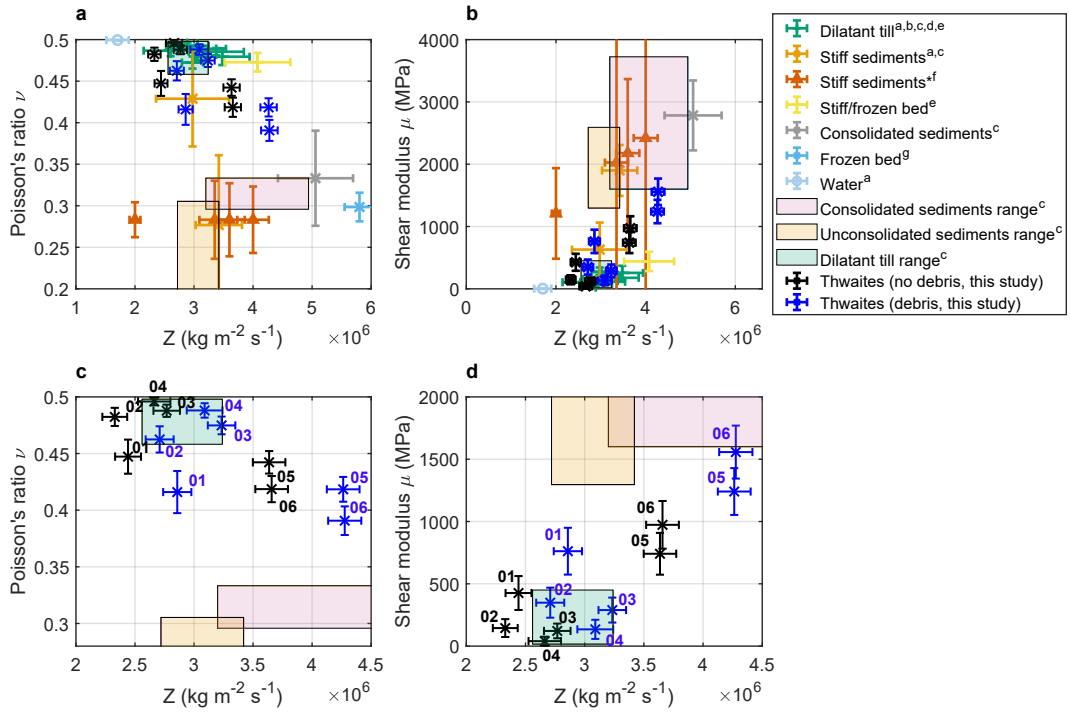

Figure 6. Results of AVA inversions (blue, black crosses) plotted alongside values from previous studies (see appendix C). Panels (a, c) show our results as medians ± half inter quartile ranges computed from marginal distributions of Z and ν; Panels (b, d) show results drawn from marginal distributions of Z and μ. Lower panels (c, d) are zoomed in views of the upper panels (a, b), with only the ranges from (Christianson et al., 2014) plotted. Results from sites AVA01-AVA06 are numbered. [a]Peters et al. (2007), [b]Peters and Anandakrishnan (2007), [c]Christianson et al. (2014), [d]Luthra et al. (2016), [e]Luthra et al. (2017), [f]Horgan et al. (2021), [g]Agnew et al. (2025). * denotes results from a study accounting for the effect of debris inclusions in basal ice.

than the tills at AVA03-AVA04, having lower ν and higher μ (Figure 6c). Despite the increased stiffness, Z at AVA01 is lower than Z at either AVA03 or AVA04. This may be indicative of complex sedimentary behavior.

Sites AVA01-AVA04 are underlain by the bedforms SED1 and SED2, which we interpret as such based on the low roughness of the interfaces and low acoustic impedances. AVA02 and AVA04 lie near to the high points of the bedforms, and show consistently higher ν and lower Z, μ than AVA01 and AVA03, respectively, which are downstream in the lee side of the sedimentary tails. The weakest till we interpret is at site AVA04, on the crest of SED2, which has a shear modulus of $\mu = 100 \pm 70$ MPa. The bed at sites AVA05 and AVA06 is stiffer and harder than the soft sediments observed downstream, with higher Z, μ and lower ν. The stiffest section of bed we image is at AVA05, with $Z = 4.28 \pm 0.14 \times 10^6$ kg m^{-2} s^{-1}, $\mu = 1.56 \pm 0.21$ GPa. These properties point toward the bed at this location being composed of stiff till or somewhat consolidated but not lithified sediments.

Table 4
AVA Inversion Results Assuming Debris-Laden Basal Ice With 10% Debris Inclusions by Volume

AVA supergather	ρ (kg m^{-3})	v_p (m s^{-1})	v_s (m s^{-1})	$Z \times 10^6$ (kg m^{-2} s^{-1})	ν	μ (GPa)	κ (GPa)
AVA01	1,530 ± 180	1,870 ± 220	700 ± 110	2.86 ± 0.12	0.42 ± 0.02	0.76 ± 0.19	4.3 ± 0.46
AVA02	1,450 ± 170	1,870 ± 220	490 ± 100	2.71 ± 0.12	0.46 ± 0.01	0.35 ± 0.12	4.6 ± 0.49
AVA03	1,700 ± 190	1,900 ± 210	410 ± 86	3.23 ± 0.12	0.47 ± 0.01	0.29 ± 0.10	5.7 ± 0.59
AVA04	1,620 ± 200	1,910 ± 220	280 ± 86	3.09 ± 0.15	0.49 ± 0.01	0.14 ± 0.08	5.7 ± 0.60
AVA05	2,120 ± 150	2,040 ± 150	860 ± 80	4.28 ± 0.14	0.39 ± 0.01	1.56 ± 0.21	6.6 ± 0.50
AVA06	2,060 ± 150	2,090 ± 140	780 ± 77	4.26 ± 0.14	0.42 ± 0.01	1.24 ± 0.19	7.2 ± 0.49

Note. Quoted uncertainties are half interquartile ranges.

21699011, 2026, 12, Downloaded from https://agupubs.onlinelibrary.wiley.com/doi/10.1029/2026JF009300 by British Antarctic Survey, Wiley Online Library on [27/11/2026]. See the Terms and Conditions (https://onlinelibrary.wiley.com/terms-and-conditions) on Wiley Online Library for rules of use; OA articles are governed by the applicable Creative Commons License

21699011, 2026, 12, Downloaded from https://agupubs.onlinelibrary.wiley.com/doi/10.1029/2026JF009300 by British Antarctic Survey, Wiley Online Library on [27/11/2026]. See the Terms and Conditions (https://onlinelibrary.wiley.com/terms-and-conditions) on Wiley Online Library for rules of use; OA articles are governed by the applicable Creative Commons License

Table 5
Combinations of VGS Parameters Consistent With AVA Data

Range	N (kPa)	ϕ	d (mm)	$d*N$ (Pa m)
Full grid search	0–5,000	0.35–0.65	0.001–1	0–5,000
AVA03/04 Sieve (soft sediment)	20–5,000	0.43–0.64	0.001–1	1.5–30
AVA05/06 Sieve (stiff sediment)	160–5,000	0.39–0.57	0.028–1	140–370

Note. "Full grid search" refers to the ranges from which sediment properties were predicted. "Sieve" rows show ranges remaining when all models predicting Z, ν and μ outside the uncertainties of our AVA inversion are excluded.

4.3. VGS-AVA Results

The locations used for VGS sieving encompass both soft sediment (AVA03/04) and stiff sediment (AVA05/06) regimes, interpreted from the acoustic impedance and AVA analyses. dN for AVA05/06 is higher than for AVA03/04, with no overlap between the results for the two regions (Table 5; Figure 7). VGS sieving indicates the porosity of the soft sediment at AVA03/04 (SED2) is 0.43−0.65. Given observed porosities of subglacial tills elsewhere in Antarctica (e.g., Kamb, 2001), we expect the true porosity to be at the lower end of this range (∼0.44). The stiffer area, AVA05/06, has a less elevated porosity of 0.39−0.57. Again, our VGS sieving allowed a broad range of possible values, so we expect the true porosity to be at the lower end of this range. The large overlap in porosities and large spread of allowed values means that we are unable to constrain this further.

In contrast to the overlap in allowed porosities, there is no overlap in the ranges of dN left after sieving for the two areas. The soft sediment has limits of $1.5 \leq dN \leq 30$ Pa m, and the stiff sediment has limits of $140 \leq dN \leq 370$ Pa m. The difference in dN can be explained by (a) a change in grain size, (b) a change in effective pressure, or (c) a combination of the two over the 2−4 km distance between the two sites. The VGS sieving puts a lower limit on effective pressure at AVA03/04 of 20 kPa. However, note that this is the first grid point, so effective pressures approaching zero may be consistent with the data here. N close to zero would be consistent with very weak, deforming till, or possibly decoupling between the ice and bed (e.g., Iverson et al., 1995). At AVA05/06, the lower limit for N is 160 kPa. If the sediment grain size distribution is similar at the two sites, these results suggest that the difference in reflectivity may be attributable to differences in effective pressure.

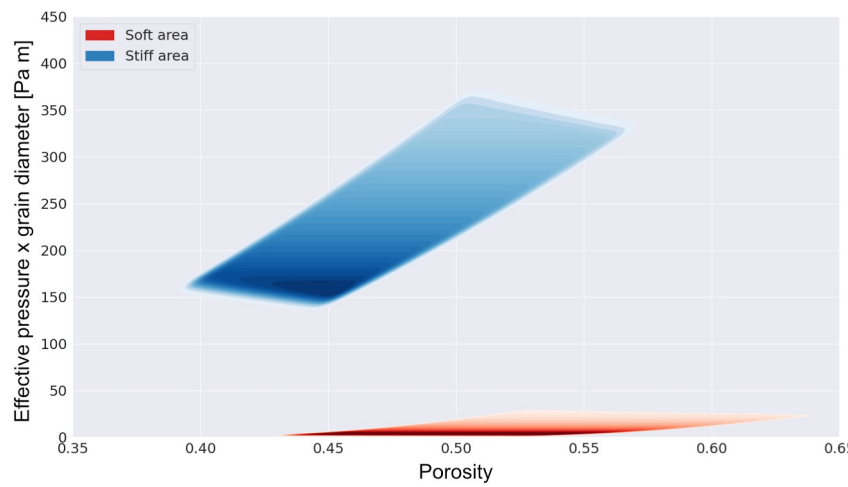

Figure 7. Results of VGS sieving for soft sediments AVA03/04 (red) and stiff sediments at AVA05/06 (blue). Shading indicates density of model combinations remaining after sieving (darker = higher probability density).

21699011, 2026, 12, Downloaded from https://agupubs.onlinelibrary.wiley.com/doi/10.1029/2026JF009300 by British Antarctic Survey, Wiley Online Library on [27/11/2026]. See the Terms and Conditions (https://onlinelibrary.wiley.com/terms-and-conditions) on Wiley Online Library for rules of use; OA articles are governed by the applicable Creative Commons License

5. Discussion

5.1. Ice Dynamics

Our results are consistent with previous studies on Thwaites Glacier which have found hard-bedded stoss and soft-bedded lee sides of bedforms (Clyne et al., 2020; Muto, Anandakrishnan, et al., 2019; Zeising et al., 2026). Our interpretation that this section of bed is composed of sediments also aligns with the result of Borthwick et al. (2025), who interpreted the presence of a sedimentary basin upstream of our field site that thins as it approaches Ghost Ridge. The bedform SED1 has a height of 5−10% of ice thickness H and a lateral scale of ∼1 ice thickness ($H \sim 2{,}100$ m at this location). This scale is similar to other crag and tails on Thwaites Glacier (Clyne et al., 2020; Muto, Anandakrishnan, et al., 2019; Zeising et al., 2026).

The observation of heterogeneous bed conditions in our study and those of previous authors has ice dynamic implications. Fast flow of ice streams is generally associated with some combination of low effective pressures, deforming till, or uncoupling of ice from the underlying till. Hard or frozen beds are generally associated with slower flow. However, the processes governing unstable evolution of ice streams such as Thwaites Glacier and their grounding line retreat are complex, and fast flow facilitated by a locally soft bed in the short term does not necessarily lead to a greater loss of ice over the whole catchment on decadal or centennial timescales. This is because ice flow over a heterogeneous bed can involve nonlinear processes resulting in grounding line retreat rates outside the endmembers for uniform hard or soft beds (Koellner et al., 2019; Schwans et al., 2026), making it difficult to infer the ice dynamic consequences of our observations without detailed modelling. Models that include spatially variable sliding laws are therefore important for understanding Thwaites Glacier's dynamics in the context of the highly heterogeneous bed observed. Most models do not account for this spatial variability, or subsume it into the drag coefficient in a Weertman-type sliding law retrieved from an inversion, therefore not representing the full physics of the ice-bed interface variability (see Brondex et al., 2017). Next-generation models should aim to portray this more accurately, informed by geophysical observations.

5.2. Subglacial Porosity and Effective Pressure

The limits on porosity, effective pressure and dN given by the AVA-VGS analysis indicate that variations in reflectivity of the ice-bed interface are controlled by variations in both porosity and effective pressure. This agrees with recent laboratory ring-shear experiments testing the dependence of R_0 on porosity and effective pressure against predictions from VGS theory (Hansen, Zoet, & Muto, 2024; Hansen, Warburton, et al., 2024). Our study is the first time to the authors' knowledge that VGS theory has been combined with glacial AVA data to constrain bed properties and effective pressure. Our conclusion that the effective pressure is likely to vary across our survey region supports the use of a spatially variable effective pressure in ice sheet models.

In an analysis of 11 Antarctic tills, Zoet et al. (2026) found that the grain size distribution varies less from till to till than do other factors such as hydraulic conductivity and coefficient of consolidation. While tills vary in makeup, the comminution process to which they are subject causes tills to mature over long transport distances. The exception to this is if the tills are entirely sourced from marine muds, which is likely not the case for Thwaites because of the subglacial highlands present upstream of the present study site which must be eroding (Clyne et al., 2020; Muto, Anandakrishnan, et al., 2019). This erosion is likely to result in the tills underlying our study site displaying a full spectrum of grain sizes and being relatively homogeneous along our profile. We therefore consider it a reasonable assumption that the grain size distribution is similar at AVA03/04 and AVA05/06, meaning that the difference in dN between the two sites is primarily controlled by differences in effective pressure.

While it is not possible with our data to constrain the grain size distribution, we can illustrate the sensitivity of the effective pressure to the constraint of dN by assuming a median grain diameter of $d_{50} = 0.13$ mm, which is consistent with a sediment core retrieved from Rutford Ice Stream (Hank et al., 2026, supplement). Using the limits of dN in Table 5 with this grain size, the limits of effective pressure are $12 < N_{\text{soft}} < 230$ kPa for the soft sediment and $1{,}080 < N_{\text{stiff}} < 2{,}900$ kPa for the stiff sediment. If this grain size is representative of both areas, there is an effective pressure difference of at least a few hundred kPa, and possibly on the order of

MPa between the soft and stiff areas. Effective pressure changes of the order MPa support previous modelling; Alley et al. (2021) modelled hemispherical bedrock bumps of 100 m height which resulted in differences of ~2 MPa between the stoss and lee sides of the bumps for flow speeds of 100 m a^{-1} and ice thicknesses of 2 km. The change in effective pressure we infer does not appear to originate from the along-profile subglacial topography, so it may be a result of the 3-dimensional topography of the ice bed and/or changes in the subglacial hydrological system. This magnitude of effective pressure change would imply low water pressures and a very active subglacial drainage system, contrary to the conventional understanding of Antarctic ice stream beds as being close to floatation everywhere. Further work is necessary to understand more fully the limitations of the AVA-VGS approach, where it may be most effective, and whether the implication of an active hydrological system here is reliable.

Direct measurements from borehole access at Rutford Ice Stream found effective pressures of 168–204 kPa, with similar N measured at sites where both soft and stiff sediments had been interpreted from geophysical data (Smith et al., 2021). This is within the limits of N_{soft} at Thwaites Glacier implied by $d_{50} = 0.13$ mm. The observations from Rutford Ice Stream contradict our interpretation that effective pressure is likely to be higher over the stiff sediments, suggesting that behavior of these sediments may be complex. We are not able to provide upper limits on N independent of grain size, so the possibility that effective pressures are similar where we interpret soft and stiff sediments cannot be excluded.

The porosities predicted by VGS at both of these sites include high values compared to laboratory results and in situ observations. The porosity implied by the VGS sieving for the stiff area is within the range of porosities observed in situ for dilatant till, which contradicts our interpretation (Kamb, 2001). However, we do not change our interpretation that the bed is stiff here and instead suggest that the VGS sieving results in overestimates of sediment porosity. This may result from systematic errors in the seismic processing and AVA inversion. For example, if our assumption of 10% entrained debris was an underestimate, this would lead to an overestimate of porosity in the VGS analysis and changes in the limits of effective pressures. An in-depth sensitivity analysis is beyond the scope of this paper; however, to illustrate the impact varying debris content has on the AVA-VGS analysis, Appendix B shows results of the VGS sieving on clean-ice derived AVA results, comparable to Figure 7. Alternatively, the inconsistency between our AVA-VGS results and in situ observations could indicate that VGS theory needs further adaptation before it is widely applicable to the subglacial system. Direct access to the subglacial system at the time of shooting is desirable to determine the extent to which each of these is the case.

Porosity and effective pressure are related: under increasing effective pressure, a till would undergo consolidation and a lowering of porosity if water is able to exit the pore space. The response of a till to changes in effective pressure is controlled by the hydraulic permeability of the till (Morgan-Witts et al., 2025). Laboratory studies indicate deforming tills undergo relatively small changes in porosity when subject to effective pressure increases of a few hundred kPa (Hansen, Zoet, & Muto, 2024; Hansen, Warburton, et al., 2024). The acoustic impedances we observe, while ruling out strongly lithified material, are not inconsistent with some sediment consolidation in the stiff bed areas, with the higher effective pressures accompanied by a lowering of porosity. Again, the wide range and overlap of porosities predicted by VGS means that we are unable to constrain this.

There are other possible explanations for the difference in reflectivity which we are not able to exclude using only our data. For example, the stiffer and rougher bed area could be composed of heterogeneous bedforms with lithified sediment outcrops and soft sediment tails, on a lateral scale smaller than the Fresnel zone. This may lead to an observed reflection coefficient consistent with stiff sediments, but where the bed violates the assumptions of VGS, which is applicable to unlithified saturated granular sediments. Synthetic seismic modelling is necessary to determine the extent to which small-scale bedforms could impact interpretations such as these.

21699011, 2026, 12, Downloaded from https://agupubs.onlinelibrary.wiley.com/doi/10.1029/2026JF009300 by British Antarctic Survey, Wiley Online Library on [27/11/2026]. See the Terms and Conditions (https://onlinelibrary.wiley.com/terms-and-conditions) on Wiley Online Library for rules of use; OA articles are governed by the applicable Creative Commons License

5.3. Basal Dynamics

Variations in effective pressure such as those inferred here would spatially alter the slip dynamics of the glacier. The regularized Coulomb slip law proposed by Zoet and Iverson (2020) for deformable beds and demonstrated as applicable to debris-rich basal ice by Hansen, Warburton, et al. (2024), would indicate a linearly proportional change in the basal drag with changes in N. Spatial variations in N would cause spatial variations in drag, altering the movement of the overriding ice. The use of seismics to first classify the bed, which in this case consists of sediments, along the "soft" and "hard" spectrum, limits the choice of the slip law, providing a much needed first constraint. Then, the use of the VGS method to provide estimates of N helps to constrain perhaps the second largest source of uncertainty in slip estimates, addressing two of the biggest unknowns with a single data set.

The correlation of imaged bedforms with the estimated values of N also indicates a link between sediment transport rates and basal properties. Spatially varying N values alter the flux of subglacial sediment, as it has been shown to depend on effective pressure (Damsgaard et al., 2020; Hansen & Zoet, 2022). Hansen and Zoet (2022) showed via laboratory experiments that sediment flux depends non-monotonically on the value of N for a given slip speed. A sediment flux law based on these findings with a dependence on N was proposed in Schlegel et al. (2025), where it was successfully able to capture regions of bed deformation and non-deformation that were inferred from seismic and radar data at Rutford Ice Stream. The spatial heterogeneity in N could lead to spatially varying divergence and convergence of sediment fluxes for different regions of the bed. This is consistent with our observations: according to this model of sediment flux, the region with higher N (AVA05/06) will have a greater sediment flux than regions with lower N (AVA03/04). The sediment flux on the stoss side of these features will be greater than the sediment flux out of the lee side, leading to net deposition of the sediment in the areas of our profile where we infer the presence of soft sediments.

Where soft beds are inferred from Z_b, motion is commonly assumed to be dominated by pervasive till deformation; however, as noted before, direct observations have shown ice sliding over soft till beds with little till deformation (Engelhardt & Kamb, 1998; Iverson et al., 1995). Alley et al. (2021) framed till behavior in terms of whether sediment flux increases or decreases with increasing effective pressure. They noted that at very low effective pressure, raising the water pressure by adding more water floats the ice off the till and decreases sediment flux, but at very high effective pressure, till is rigid and raising the water pressure by adding more water can allow deformation and increase sediment flux. In this context, the hard and soft regions in our profile may be distinguished by opposite sediment flux responses to increasing water supply as well as different sediment fluxes.

5.4. Geomorphic Implications

Our data advance earlier work showing that the bed alternates between harder materials and soft tills with high porosity and high water pressure (Clyne et al., 2020; Muto, Anandakrishnan, et al., 2019; Zeising et al., 2026). The soft tills occur over extensive basins and at the crests of mega-scale glacial lineations (MSGLs) in lee-side positions of large obstacles. The harder materials occur on stoss sides of obstacles, in moats upstream of obstacles and their extensions between the MSGLs, and across subglacial highlands (see Holschuh et al., 2020; Muto, Alley, et al., 2019). We find the softest till at the crest of the bedform SED1, which is consistent with properties inferred from seismic and radar observations at Rutford Ice Stream, where the softest material was found at bedform crests (Schlegel et al., 2022). Our observation of SED2 developing not in the lee of pronounced topography but an undulating harder section suggests that sedimentary bedforms may form in response to hydrologically as well as geometrically driven differences in effective pressure. The data of Zeising et al. (2026) point to harder material in MSGLs beneath their soft ice-contact till, suggesting that the bedforms we observe are both erosional and depositional. Continuing erosion might someday lower the obstacles that produce lee-side MSGLs, leaving MSGLs that are largely or completely erosional (see Alley et al., 2022).

The results here contribute to furthering our understanding of the geomorphic processes and history beneath Thwaites Glacier and surroundings. Like other ice sheets, the West Antarctic Ice Sheet is erosive overall (Pollard & DeConto, 2020; Wilson et al., 2012), generating and transporting material that is deposited in grounding-zone

21699011, 2026, 12, Downloaded from https://agupubs.onlinelibrary.wiley.com/doi/10.1029/2026JF009300 by British Antarctic Survey, Wiley Online Library on [27/11/2026]. See the Terms and Conditions (https://onlinelibrary.wiley.com/terms-and-conditions) on Wiley Online Library for rules of use; OA articles are governed by the applicable Creative Commons License

21699011, 2026, 12, Downloaded from https://agupubs.onlinelibrary.wiley.com/doi/10.1029/2026JF009300 by British Antarctic Survey, Wiley Online Library on [27/11/2026]. See the Terms and Conditions (https://onlinelibrary.wiley.com/terms-and-conditions) on Wiley Online Library for rules of use; OA articles are governed by the applicable Creative Commons License

wedges or as dropstone diamictons beyond the grounding zone, and eventually moved over the continental shelf edge during major glacial advances. Soft tills generally suppress erosion (e.g., Cuffey & Alley, 1996). Some transport of sediment is possible when unlithified material beneath soft tills is entrained into an ice-contact deforming layer. The widespread erosion indicated by proglacial deposits is likely dominated by sources in harder-bedded regions. The harder-bed acoustic impedances measured in recent studies point to somewhat-lithified sedimentary rocks from preglacial or interglacial times, with little to no evidence for crystalline bedrock or strongly lithified sedimentary rock in contact with the ice (e.g., Borthwick et al., 2025; Clyne et al., 2020; Muto, Anandakrishnan, et al., 2019; Muto, Alley et al., 2019; Zeising et al., 2026). Results of coring beneath the Amundsen Sea in the paleo-drainage basins of Thwaites and Pine Island glaciers are fully consistent with the inferences of erosion of somewhat-lithified sedimentary rocks. The coring recovered Cretaceous to Eocene fluvial sedimentary deposits, and younger (Miocene, Pliocene and perhaps Pleistocene) unlithified preglacial or interglacial submarine deposits in basins, as well as finding extensive kaolinite that could have come from the fluvial deposits (Gohl et al., 2017; Horikawa et al., 2026; Marschalek et al., 2025; Passchier et al., 2025).

The AVA data in our study indicate that the material in the hard-bedded region of AVA05/06 is a stiff till or somewhat consolidated sediment rather than lithified sedimentary rock. In the context of previous studies, these observations point to a mosaic of bed characters beneath Thwaites Glacier consisting of depositional soft till regions, stiff till, and eroding sedimentary rock in subglacial highlands and the stoss side of obstacles.

Opportunities exist for further research targeting these hypotheses, using co-located seismics and swath radar, and eventually guiding coring into representative bed types to confirm the remote geophysics. For now, erosion and deposition are rather clearly interacting in ways that produce moats, MSGLs, and other features observed beneath Thwaites Glacier.

5.5. Methodological Implications

Collecting normal-incidence data to estimate basal acoustic impedances is logistically easier than collecting AVA data. The rationale for inferring hard-bedded and soft-bedded areas based on acoustic impedance is that shear modulus correlates with the acoustic impedance of the bed. Broadly, when comparing classes of stiff and soft beds, our results are in accord with this (Figure 6); the bed at AVA05/06 has both higher Z and μ than the tills inferred at AVA01-04. However, comparing soft tills from SED1 (lower Z, higher μ) and SED2 (higher Z, lower μ) suggests that for deformable tills, sediment properties are determined by complex interactions between the sediment grains, the overburden pressure and shear stress imposed by ice, and the subglacial hydrological system. The explicit inclusion of effective pressure variations in slip laws means that this should be considered when interpreting seismic data.

Our results, which assume the basal ice is debris-laden, show uniformly higher Z, lower ν and higher μ than results obtained without basal debris. Recent work using data from Rutford Ice Stream, which inferred bed shear modulus from passive seismic data and compared this to active seismic-derived acoustic impedances, has suggested that ice stream beds may be stiffer than previously thought (Hudson et al., 2025). This could result from active seismic surveys on ice streams across Antarctica to date having used incorrect assumptions about the properties of basal ice. Figure 4 underscores this, with some acoustic impedances using the clean-ice assumption falling below the likely acoustic impedances of soft till. Furthermore, the very high porosities implied by VGS-AVA highlights that standard glaciological seismic processing workflows may result in underestimates of Z and μ (causing VGS-AVA sieving to overestimate sediment porosity). Alternatively, the high apparent porosity could result from the limitations of the VGS-AVA approach itself; further work is needed to determine whether this is the case, and the approach may need to be refined in future.

Qualitative interpretation of hard and soft-bedded areas is likely to be robust to these limitations. However, if models aim to include seismic data quantitatively for the constraint of sliding laws, assumptions of basal ice properties and their effect on the estimated stiffness of the ice stream bed may have to be further quantified. Field campaigns that include geophysical surveys simultaneously with direct access to the subglacial system are highly desirable to calibrate these methods (e.g., Smith et al., 2021); this will improve the suitability of data products for constraining ice sheet models.

6. Conclusions

We image a section of the bed of Thwaites Glacier immediately upstream of Ghost Ridge, 65 km from the current Thwaites Glacier grounding zone, and use the seismic reflectivity of the ice-bed interface to investigate bed properties. This section of Thwaites Glacier is underlain by a layer of subglacial sediment. The sediment is spatially variable, with areas of stiff sediments interspersed with areas of soft sediments. We do not observe a clear reflection from the base of the sediment. We image a crag and tail formation of approximately 130 m relief from the surrounding area, with a hard bed on its stoss side and soft till on its lee side. We also find soft till in the lee of an undulating area of stiff sediments. The varied bed conditions reported in this and previous studies may mean different sections of the bed are best described by different sliding laws; this may have ice dynamic implications.

We use seismic amplitude-versus-angle (AVA) analysis to constrain the shear properties of the interface, resulting in improved estimates of subglacial acoustic impedance, Poisson's ratio and shear modulus. Comparison of soft and stiff areas of the bed using a novel combination of AVA analysis and viscous grain shearing (VGS) theory constrains the ranges of effective pressure and porosity for these contrasting areas of the bed. Variations in seismic reflectivity along our profile are likely to be controlled by variations in both subglacial effective pressure and porosity. This study is the first time to the authors' knowledge that VGS theory has been applied to glacial AVA data to support this conclusion, and the observation is in agreement with recent laboratory studies. Estimated bed properties are sensitive to the assumed properties of the ice base; future work should aim to further constrain assumptions about basal ice properties and update ranges of acoustic impedance considered consistent with different subglacial regimes. Major field projects in the future should aim to constrain bed properties by direct access at the time of shooting, enabling quantitative integration of complementary active seismic data sets and confirming the applicability of VGS to seismic AVA surveys.

Appendix A: Viscous Grain Shearing Theory: Governing Equations

Viscous Grain Shearing (VGS) theory (Buckingham, 1997, 2005, 2007) predicts the seismic compressional and shear wave velocities v_p, v_s of an unconsolidated granular saturated sediment, as a function of effective pressure N, grain diameter d_g, porosity ϕ, and seismic frequency f_s. The governing equations are given here. See Hank et al. (2026) for a fuller description of VGS as applied to subglacial sediments. Subscripts "0" refer to quantities in the absence of grain-to-grain interactions. The wave speeds are given by:

$$v_p = \frac{c_0}{\mathrm{Re}[1 + \zeta(i\omega T)^q g(\omega\tau_p)]^{-1/2}} \tag{A1}$$

$$v_s = \frac{\sqrt{\gamma_s/\rho_0}}{\mathrm{Re}[(i\omega T)^q g(\omega)]^{1/2}} \tag{A2}$$

ζ is the dimensionless grain-shearing coefficient, which is determined by the compressional and shear rigidity coefficients γ_p and γ_s:

$$\zeta = \frac{\gamma_p + (4/3)\gamma_s}{\rho_0 c_0^2}, \tag{A3}$$

$$\gamma_p = \gamma_{p0}\left[\frac{N d_g}{N_0 d_{g0}}\right]^{1/3}, \tag{A4}$$

$$\gamma_s = \gamma_{s0}\left[\frac{N d_g}{N_0 d_{g0}}\right]^{2/3}. \tag{A5}$$

The function $g(\omega\tau_p)$ accounts for the effect of the viscosity ν of the molecularly thin layer of pore fluid between grains. $\tau_p = \nu/E$ is the compressional viscoelastic time constant, and E is a spring constant. We use $\tau_p = 0.012$ as adjusted for the ice overburden pressure as in Hank et al. (2026). q is the strain hardening index.

21699011, 2026, 12, Downloaded from https://agupubs.onlinelibrary.wiley.com/doi/10.1029/2026JF009300 by British Antarctic Survey, Wiley Online Library on [27/11/2026]. See the Terms and Conditions (https://onlinelibrary.wiley.com/terms-and-conditions) on Wiley Online Library for rules of use; OA articles are governed by the applicable Creative Commons License

v_0 is the P-wave velocity in the absence of grain-to-grain interactions, and is determined by the bulk modulus κ_0 and density ρ_0:

$$v_0 = \sqrt{\frac{\kappa_0}{\rho_0}}. \tag{A6}$$

The bulk modulus of the medium is given by

$$\kappa_0 = \left(\frac{\phi}{\kappa_p} + \frac{1-\phi}{\kappa_g}\right)^{-1}. \tag{A7}$$

The bulk density is

$$\rho_0 = \phi\rho_p + (1-\phi)\rho_g. \tag{A8}$$

κ_0, ρ_0 are the bulk modulus and density in the absence of grain-to-grain interactions, κ_p, ρ_p are the bulk modulus and density of the pore fluid, and κ_g, ρ_g are the bulk modulus and density of the grains. $\omega = 2\pi f$ is the angular frequency. $i = \sqrt{-1}$. We use $f_s = 200$ Hz to match the dominant frequency of our ice-base reflection, and assume grains are composed of quartz: $\rho_g = 2{,}650$ kg m^{-3}, $\kappa_g = 3.66 \cdot 10^{10}$ Pa (Mavko et al., 2009). All other parameters are the same as in Hank et al. (2026) and are listed in Table A1.

Table A1
Parameters Used in VGS Calculations

Symbol	Description	Value	Unit
T	Arbitrary time introduced to avoid awkward dimensions	1	s
q	Strain hardening index	0.0851	–
κ_p	Bulk modulus of pores	$2.374 \cdot 10^9$	Pa
κ_g	Bulk modulus of grains	$3.66 \cdot 10^{10}$	Pa
ρ_p	Density of pore fluid	1,005	kg m^{-3}
ρ_g	Density of grains	2,650	kg m^{-3}
γ_{p0}	Reference compressional coefficient	$3.888 \cdot 10^8$	Pa
γ_{s0}	Reference shear coefficient	$4.588 \cdot 10^7$	Pa
d_{g0}	Reference grain diameter	$1 \cdot 10^{-3}$	m
ϕ_0	Reference porosity	0.377	–
g	Acceleration due to gravity	9.81	m s^{-2}
z_0	Reference depth in sediment	0.3	m
f_s	Seismic frequency	200	Hz
τ_p	Compressional viscoelastic time constant	0.012	s

Note. All Parameters are as in Hank et al. (2026), with the exception of the seismic frequency f_s and the bulk modulus and density of grains κ_g, ρ_g. We adjust f_s to match the dominant frequency of our ice-base reflection ($f_s = 200$ Hz), and Assume grains are composed of quartz ($\rho_g = 2{,}650$ kg m^{-3}, $\kappa_g = 3.66 \cdot 10^{10}$ Pa).

21699011, 2026, 12, Downloaded from https://agupubs.onlinelibrary.wiley.com/doi/10.1029/2026JF009300 by British Antarctic Survey, Wiley Online Library on [27/11/2026]. See the Terms and Conditions (https://onlinelibrary.wiley.com/terms-and-conditions) on Wiley Online Library for rules of use; OA articles are governed by the applicable Creative Commons License

Appendix B: Results for Clean Basal Ice

Table B1 contains results from AVA analysis of the responses at AVA01-06, as displayed by the black data points in Figure 6. We also include here the results of VGS sieving for the clean basal-ice derived AVA results. Figure B1 shows the results of VGS sieving for the regions AVA03/04 ("soft area") and AVA05/06 ("stiff area"). In the clean ice assumption case, the limits on porosity for the stiff area are $0.47 \leq \phi \leq 0.65$ and the limits on dN are $60 \leq dN \leq 210$ Pa m. The lower limit on porosity for the soft area is 0.57 and the upper limit lies outside our searched area. $dN < 10$ Pa m for the soft area. Comparing Figure B1 with Figure 7 indicates the sensitivity of the VGS sieving method to the basal debris assumption. When the basal debris concentration is increased in the AVA inversion, the porosities consistent with VGS decrease, and the limits of dN increase.

Table B1
AVA Inversion Results if Basal Ice is Assumed Clean

AVA supergather	ρ (kg m^{-3})	v_p (m s^{-1})	v_s (m s^{-1})	$Z \times 10^6$ (kg m^{-2} s^{-1})	ν	μ (GPa)	K (GPa)
AVA01	1,320 ± 150	1,850 ± 210	560 ± 110	2.44 ± 0.11	0.45 ± 0.02	0.43 ± 0.14	3.9 ± 0.42
AVA02	1,250 ± 140	1,860 ± 200	340 ± 90	2.33 ± 0.11	0.48 ± 0.008	0.15 ± 0.08	4.1 ± 0.45
AVA03	1,470 ± 170	1,880 ± 210	290 ± 80	2.77 ± 0.11	0.49 ± 0.005	0.12 ± 0.06	5.0 ± 0.54
AVA04	1,390 ± 160	1,920 ± 210	170 ± 80	2.66 ± 0.14	0.50 ± 0.003	0.04 ± 0.04	5.0 ± 0.54
AVA05	1,920 ± 210	1,910 ± 210	710 ± 100	3.66 ± 0.14	0.42 ± 0.01	0.97 ± 0.19	5.7 ± 0.56
AVA06	1,840 ± 200	1,990 ± 210	640 ± 100	3.64 ± 0.14	0.44 ± 0.01	0.74 ± 0.17	6.2 ± 0.58

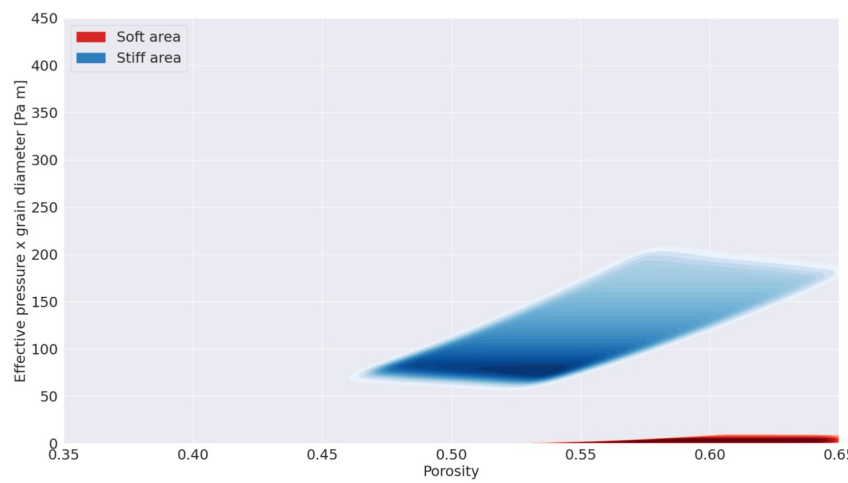

Figure B1. Results of VGS sieving for soft sediments AVA03/04 (red) and stiff sediments at AVA05/06 (blue), for the clean basal ice assumption. Shading indicates density of model combinations remaining after sieving (darker = higher probability density).

Appendix C: Previously Published Glaciological AVA Results

Table C1

21699011, 2026, 12, Downloaded from https://agupubs.onlinelibrary.wiley.com/doi/10.1029/2026JF009300 by British Antarctic Survey, Wiley Online Library on [27/11/2026]. See the Terms and Conditions (https://onlinelibrary.wiley.com/terms-and-conditions) on Wiley Online Library for rules of use; OA articles are governed by the applicable Creative Commons License

Journal of Geophysical Research: Earth Surface

10.1029/2026JF009300

Table C1
Table of AVA Results by Previous Authors, Which are Plotted Alongside AVA Results Reported in This Paper

Paper	Location	V_p (m s^{-1})	V_s (m s^{-1})	ρ (kg m^{-3})	$Z \times (10^6)$ (kg m^{-2} s^{-1})	ν	μ (MPa)	K (MPa)	Interpretation
Peters et al. (2007)	Bindschadler Ice Stream	1,800 ± 150	1,000 ± 100	1,900 ± 150	3.42 ± 0.39	0.277 ± 0	1,900 ± 410	3,620 ± 1,100	Stiff sediment
Peters et al. (2007)	Bindschadler Ice Stream	1,650 ± 150	200 ± 50	1,750 ± 150	2.89 ± 0.36	0.493 ± 0.0017	70.0 ± 36	4,670 ± 870	Dilatant till
Peters et al. (2007)	Bindschadler Ice Stream	1,550 ± 100	50 ± 50	1,100 ± 100	1.71 ± 0.19	0.499 ± 0.000067	2.75 ± 5.5	2,640 ± 340	Water
*Horgan et al. (2021)	Whillans Ice Stream	2,000 ± 140	1,100 ± 300	1,800 ± 30	3.60 ± 0.26	0.283 ± 0.18	2,178 ± 1,200	4,300 ± 1,900	Stiff sediment
*Horgan et al. (2021)	Whillans Ice Stream	2,000 ± 150	1,100 ± 830	1,675 ± 30	3.35 ± 0.26	0.283 ± 0.47	2,030 ± 3,100	4,000 ± 4,200	Stiff sediment
*Horgan et al. (2021)	Whillans Ice Stream	2,000 ± 70	1,100 ± 330	1,000 ± 30	2.00 ± 0.092	0.283 ± 0.19	1,210 ± 730	2,390 ± 1,010	Stiff sediment
*Horgan et al. (2021)	Whillans Ice Stream	2,000 ± 130	1,100 ± 630	2,000 ± 30	4.00 ± 0.27	0.283 ± 0.36	2,420 ± 2,800	4,770 ± 3,840	Stiff sediment
Luthra et al. (2017)	Kamb Ice Stream	2,090 ± 200	475 ± 80	1,950 ± 190	4.08 ± 0.56	0.473 ± 0.011	440 ± 150	7,930 ± 1,640	Stiff/Frozen
Luthra et al. (2017)	Kamb Ice Stream	1,550 ± 0	250 ± 50	1,680 ± 200	2.60 ± 0.46	0.487 ± 0.0065	105 ± 44	3,900 ± 1,040	Dilatant till
Luthra et al. (2017)	Whillans Ice Stream	1,840 ± 180	310 ± 34	1,835 ± 180	3.38 ± 0.47	0.485 ± 0.0044	176 ± 42	5,980 ± 1,220	Dilatant till
Luthra et al. (2017)	Whillans Ice Stream	1,860 ± 0	370 ± 80	1,870 ± 190	3.48 ± 0.46	0.479 ± 0.010	256 ± 110	6,130 ± 1,120	Dilatant till
Peters and Anandakrishnan (2007)	Kamb Ice Stream	1,750 ± 25	400 ± 50	1,700 ± 100	2.98 ± 0.18	0.472 ± 0.0073	272 ± 70	4,840 ± 174	Dilatant till
Agnew et al. (2025)	Korff Ice Rise	−−	−−	−−	5.80 ± 0.25	0.298 ± 0.017	6,720 ± 470	14,400 ± 760	Frozen
Christianson et al. (2014)	North-East Greenland Ice Stream, Site C	1,700 ± 250	250 ± 150	1,800 ± 100	3.06 ± 0.48	0.489 ± 0.014	113 ± 135	5,050 ± 1,540	Dilatant till
Christianson et al. (2014)	North-East Greenland Ice Stream, Site D	1,700 ± 200	600 ± 200	1,750 ± 300	2.98 ± 0.62	0.429 ± 0.057	630 ± 430	4,220 ± 1,320	Stiff sediment
Christianson et al. (2014)	North-East Greenland Ice Stream, Site E	2,199 ± 200	1,100 ± 100	2,300 ± 200	5.06 ± 0.64	0.333 ± 0.057	2,780 ± 560	7,410 ± 2,130	Consolidated sediment

Note. *Denotes results from a study accounting for the effect of debris inclusions in basal ice.

21699011, 2026, 12, Downloaded from https://agupubs.onlinelibrary.wiley.com/doi/10.1029/2026JF009300 by British Antarctic Survey, Wiley Online Library on [27/11/2026]. See the Terms and Conditions (https://onlinelibrary.wiley.com/terms-and-conditions) on Wiley Online Library for rules of use; OA articles are governed by the applicable Creative Commons License

Conflict of Interest

The authors declare no conflicts of interest relevant to this study.

Availability Statement

Data are archived with the UK Polar Data Centre (Agnew et al., 2026). AVA inversions were carried out in MATLAB. AVA inversion code can be accessed at Zenodo (Agnew, 2025).

Acknowledgments
This work was funded through the GHOST project, a component of the International Thwaites Glacier Collaboration (ITGC). Support from National Science Foundation (NSF: Grant NSF-NERC-PLR-1738934) and Natural Environment Research Council (NERC: Grant NE/S006672/1). ITGC Contribution No. ITGC-166. Logistics were provided by NSF-U.S. Antarctic Program and NERC-British Antarctic Survey. Seismic data were processed with Halliburton-Landmark ProMAX software under academic license to British Antarctic Survey. We are grateful to Catrin Thomas for support in the field; Tanner Kuhl and Barbara Birrittella for hot water drilling support and assisting with data acquisition. We thank James Smith for helpful discussions. We thank Anya Reading, Martin Truffer and an anonymous reviewer, as well as the editors, for feedback which improved the paper. Members of the GHOST collaboration are: Ronan Agnew, Richard Alley, Sridhar Anandakrishnan, Robert Arthern, Robert Bingham, Julien Bodart, Louise Borthwick, Alex Brisbourne, Elizabeth Case, Knut Christianson, Olaf Eisen, Kevin Hank, Andrew Hoffman, Coen Hofstede, Nicholas Holschuh, Siobhan Killingbeck, Jonathan Kingslake, Bernd Kulessa, Sierra Melton, Atsuhiro Muto, Felipe Napoleoni, Helen Ockenden, Rebecca Pearce, Byron R. Parizek, Kiya Riverman, Rebecca Schlegel, Emily Schwans, Andrew Smith, Leigh Stearns, Nathan Stevens, Amanda Willet, Paul Winberry, Jaiden Zak, Ole Zeising, and Lucas Zoet.

References

Agnew, R. S. (2025). Agnewr/mcmc-ava: Mcmc-ava-v1.0.2. *Zenodo*. https://doi.org/10.5281/zenodo.17901754

Agnew, R. S., Anandakrishnan, S., Brisbourne, A., Borthwick, L., Melton, S., & Willet, A. (2026). Unprocessed seismic reflection shot gathers from ghost ridge [Dataset]. *NERC EDS UK Polar Data Centre*. Thwaites Glacier, West Antarctica (2024. https://doi.org/10.5285/5923905d-edb4-459a-b744-5a684b1592fa

Agnew, R. S., Booth, A. D., Brisbourne, A. M., Clark, R. A., Livermore, P. W., & Smith, A. M. (2025). Subglacial conditions from converted-wave seismic reflection amplitudes: Synthetic experiments and case study reveal a frozen bed at an antarctic ice rise. *Journal of Geophysical Research: Earth Surface*, *130*(12), e2025JF008475. https://doi.org/10.1029/2025JF008475

Alley, R. B., Holschuh, N., Parizek, B., Zoet, L. K., Riverman, K., Muto, A., et al. (2022). Ghostly flute music: Drumlins, moats and the bed of thwaites glacier. *Annals of Glaciology*, *63*(87–89), 153–157. https://doi.org/10.1017/aog.2023.43

Alley, R. B., Cuffey, K. M., Evenson, E. B., Strasser, J. C., Lawson, D. E., & Larson, G. J. (1997). How glaciers entrain and transport basal sediment: Physical constraints. *Quaternary Science Reviews*, *16*(9), 1017–1038. https://doi.org/10.1016/S0277-3791(97)00034-6

Alley, R. B., Holschuh, N., MacAyeal, D. R., Parizek, B. R., Zoet, L., Riverman, K., et al. (2021). Bedforms of thwaites glacier, West Antarctica: Character and origin. *Journal of Geophysical Research: Earth Surface*, *126*(12), e2021JF006339. https://doi.org/10.1029/2021JF006339

Anandakrishnan, S. (2003). Dilatant till layer near the onset of streaming flow of ice stream C, West Antarctica, determined by AVO (amplitude vs offset) analysis. *Annals of Glaciology*, *36*, 283–286. https://doi.org/10.3189/172756403781816329

Arthern, R. J., Winebrenner, D. P., & Vaughan, D. G. (2006). Antarctic snow accumulation mapped using polarization of 4.3-cm wavelength microwave emission. *Journal of Geophysical Research*, *111*(D6). Retrieved from https://agupubs.onlinelibrary.wiley.com/doi/abs/10.1029/2004JD005667doi:10.1029/2004JD005667

Atre, S. R., & Bentley, C. R. (1993). Laterally varying basal conditions beneath ice streams B and C, west Antarctica. *Journal of Glaciology*, *39*(133), 507–514. https://doi.org/10.3189/S0022143000016403

Båth, M. (1974). *Developments in solid Earth geophysics: Spectral analysis in geophysics*. Elsevier Scientific Publishing Company.

Benn, D. I., & Sugden, D. E. (2020). West Antarctic ice sheet and CO2 greenhouse effect: A threat of disaster. *Scottish Geographical Journal*, *136*(1–4), 13–23. https://doi.org/10.1080/14702541.2020.1853870

Bett, D. T., Bradley, A. T., Williams, C. R., Holland, P. R., Arthern, R. J., & Goldberg, D. N. (2024). Coupled ice–ocean interactions during future retreat of West Antarctic ice streams in the Amundsen Sea sector. *The Cryosphere*, *18*(6), 2653–2675. https://doi.org/10.5194/tc-18-2653-2024

Booth, A. D., Clark, R. A., Kulessa, B., Murray, T., Carter, J., Doyle, S., & Hubbard, A. (2012). Thin-layer effects in glaciological seismic amplitude-versus-angle (AVA) analysis: Implications for characterising a subglacial till unit, russell glacier, West Greenland. *The Cryosphere*, *6*(4), 909–922. https://doi.org/10.5194/tc-6-909-2012

Borthwick, L., Muto, A., Anandakrishnan, S., Tinto, K., Agnew, R., Brisbourne, A., et al. (2025). Rift-related sedimentary basin and deeper-seated mafic intrusions modeled beneath thwaites glacier, west Antarctica: Influence on glacier dynamics. *Journal of Geophysical Research: Solid Earth*, *130*(10), e2025JB031716. https://doi.org/10.1029/2025JB031716

Boulton, G. (1979). Processes of glacier erosion on different substrata. *Journal of Glaciology*, *23*(89), 15–38. https://doi.org/10.3189/S0022143000029713

Brisbourne, A. M., Smith, A. M., Vaughan, D. G., King, E. C., Davies, D., Bingham, R. G., et al. (2017). Bed conditions of pine island glacier, west Antarctica. *Journal of Geophysical Research: Earth Surface*, *122*(1), 419–433. https://doi.org/10.1002/2016JF004033

Brondex, J., Gagliardini, O., Gillet-Chaulet, F., & Durand, G. (2017). Sensitivity of grounding line dynamics to the choice of the friction law. *Journal of Glaciology*, *63*(241), 854–866. https://doi.org/10.1017/jog.2017.51

Brondex, J., Gillet-Chaulet, F., & Gagliardini, O. (2019). Sensitivity of centennial mass loss projections of the amundsen basin to the friction law. *The Cryosphere*, *13*(1), 177–195. https://doi.org/10.5194/tc-13-177-2019

Bruggeman, D. A. G. (1937). Berechnung verschiedener physikalischer Konstanten von heterogenen Substanzen, III. Die elastischen Konstanten der quasiisotropen Mischkörper aus isotropen Substanzen (Calculation of various physical constants of heterogeneous substances, III. The elastic constants of quasi-isotropic mixtures of isotropic substances). *Annalen der Physik*, *421*(2), 160–178.

Buckingham, M. J. (1997). Theory of acoustic attenuation, dispersion, and pulse propagation in unconsolidated granular materials including marine sediments. *Journal of the Acoustical Society of America*, *102*(5), 2579–2596. https://doi.org/10.1121/1.420313

Buckingham, M. J. (2005). Compressional and shear wave properties of marine sediments: Comparisons between theory and data. *Journal of the Acoustical Society of America*, *117*(1), 137–152. https://doi.org/10.1121/1.1810231

Buckingham, M. J. (2007). On pore-fluid viscosity and the wave properties of saturated granular materials including marine sediments. *Journal of the Acoustical Society of America*, *122*(3), 1486–1501. https://doi.org/10.1121/1.2759167

Budd, W. F., Keage, P. L., & Blundy, N. A. (1979). Empirical studies of ice sliding. *Journal of Glaciology*, *23*(89), 157–170. https://doi.org/10.3189/S0022143000029804

Chandra, R., Riverman, K., Pettit, E. C., Schmerr, N. C., Carroll, G., Bailey, S. H., et al. (2025). Seismic evidence of impact breccia and unlithified sediments under hiawatha glacier. *Journal of Geophysical Research: Earth Surface*, *130*(7), e2024JF008247. https://doi.org/10.1029/2024JF008247

Christianson, K., Peters, L. E., Alley, R. B., Anandakrishnan, S., Jacobel, R. W., Riverman, K. L., et al. (2014). Dilatant till facilitates ice-stream flow in northeast Greenland. *Earth and Planetary Science Letters*, *401*, 57–69. https://doi.org/10.1016/j.epsl.2014.05.060

Christoffersen, P., Tulaczyk, S., & Behar, A. (2010). Basal ice sequences in antarctic ice stream: Exposure of past hydrologic conditions and a principal mode of sediment transfer. *Journal of Geophysical Research*, *115*(F3). https://doi.org/10.1029/2009JF001430

21699011, 2026, 12, Downloaded from https://agupubs.onlinelibrary.wiley.com/doi/10.1029/2026JF009300 by British Antarctic Survey, Wiley Online Library on [27/11/2026]. See the Terms and Conditions (https://onlinelibrary.wiley.com/terms-and-conditions) on Wiley Online Library for rules of use; OA articles are governed by the applicable Creative Commons License

Clyne, E. R., Anandakrishnan, S., Muto, A., Alley, R. B., & Voigt, D. E. (2020). Interpretation of topography and bed properties beneath thwaites glacier, west Antarctica using seismic reflection methods. *Earth and Planetary Science Letters*, *550*, 116543. https://doi.org/10.1016/j.epsl.2020.116543

Cuffey, K., & Alley, R. B. (1996). Is erosion by deforming subglacial sediments significant? (toward till continuity). *Annals of Glaciology*, *22*, 17–24. https://doi.org/10.3189/1996AoG22-1-17-24

Damsgaard, A., Goren, L., & Suckale, J. (2020). Water pressure fluctuations control variability in sediment flux and slip dynamics beneath glaciers and ice streams. *Communications Earth & Environment*, *1*(1), 66. https://doi.org/10.1038/s43247-020-00074-7

Dasgupta, R., & Clark, R. A. (1998). Estimation of *Q* from surface seismic reflection data. *Geophysics*, *63*(6), 2120–2128. https://doi.org/10.1190/1.1444505

dos Santos, T. D., Barnes, J. M., Goldberg, D. N., Gudmundsson, G. H., & Morlighem, M. (2021). Drivers of change of thwaites glacier, west Antarctica, between 1995 and 2015. *Geophysical Research Letters*, *48*(20), e2021GL093102. https://doi.org/10.1029/2021GL093102

Engelhardt, H., & Kamb, B. (1998). Basal sliding of Ice stream B, West Antarctica. *Journal of Glaciology*, *44*(147), 223–230. https://doi.org/10.3189/S0022143000002562

Engelhardt, H., & Kamb, B. (2013). Kamb ice stream flow history and surge potential. *Annals of Glaciology*, *54*(63), 287–298. https://doi.org/10.3189/2013aog63a535

Evans, D. J. A., & Hansom, J. D. (1996). The Edinburgh castle crag-and-tail. *Scottish Geographical Magazine*, *112*(2), 129–131. https://doi.org/10.1080/14702549608554461

Favier, L., Durand, G., Cornford, S. L., Gudmundsson, G. H., Gagliardini, O., Gillet-Chaulet, F., et al. (2014). Retreat of pine island glacier controlled by marine ice-sheet instability. *Nature Climate Change*, *4*(2), 117–121. https://doi.org/10.1038/nclimate2094

Franke, S., Wolovick, M., Drews, R., Jansen, D., Matsuoka, K., & Bons, P. D. (2024). Sediment freeze-on and transport near the onset of a fast-flowing glacier in East Antarctica. *Geophysical Research Letters*, *51*(6), e2023GL107164. https://doi.org/10.1029/2023GL107164

Gohl, K., Freudenthal, T., Hillenbrand, C.-D., Klages, J., Larter, R., Bickert, T., et al. (2017). MeBo70 seabed drilling on a polar continental shelf: Operational report and lessons from drilling in the Amundsen Sea embayment of west Antarctica. *Geochemistry, Geophysics, Geosystems*, *18*(11), 4235–4250. https://doi.org/10.1002/2017GC007081

Gudmundsson, G. H., Barnes, J. M., Goldberg, D. N., & Morlighem, M. (2023). Limited impact of thwaites ice shelf on future ice loss from Antarctica. *Geophysical Research Letters*, *50*(11), e2023GL102880. https://doi.org/10.1029/2023GL102880

Hank, K., Arthern, R. J., Williams, C. R., Brisbourne, A. M., Smith, A. M., Smith, J. A., et al. (2026). Inferring the ice sheet sliding law from seismic observations: A pine island glacier case study. *The Cryosphere*, *20*(1), 495–510. https://doi.org/10.5194/tc-20-495-2026

Hansen, D. D., Zoet, L. K., & Muto, A. (2024). Constraints on effective stress in subglacial tills from lab-scale ultrasonic active seismic experiments. *Agu fall meeting abstracts*, *2024*, NS33A–1207.

Hansen, D. D., Warburton, K. L. P., Zoet, L. K., Meyer, C. R., Rempel, A. W., & Stubblefield, A. G. (2024). Presence of frozen fringe impacts soft-bedded slip relationship. *Geophysical Research Letters*, *51*(12), e2023GL107681. https://doi.org/10.1029/2023GL107681

Hansen, D. D., & Zoet, L. K. (2022). Characterizing sediment flux of deforming glacier beds. *Journal of Geophysical Research: Earth Surface*, *127*(4), e2021JF006544. https://doi.org/10.1029/2021JF006544

Hastings, W. K. (1970). Monte Carlo sampling methods using markov chains and their applications. *Biometrika*, *57*(1), 97–109. https://doi.org/10.1093/biomet/57.1.97

Helanow, C., Iverson, N. R., Woodard, J. B., & Zoet, L. K. (2021). A slip law for hard-bedded glaciers derived from observed bed topography. *Science Advances*, *7*(20), eabe7798. https://doi.org/10.1126/sciadv.abe7798

Hofstede, C., Eisen, O., Diez, A., Jansen, D., Kristoffersen, Y., Lambrecht, A., & Mayer, C. (2013). Investigating englacial reflections with vibro- and explosive-seismic surveys at halvfarryggen ice dome, Antarctica. *Annals of Glaciology*, *54*(64), 189–200. https://doi.org/10.3189/2013AoG64A064

Holland, C. W., & Anandakrishnan, S. (2009). Subglacial seismic reflection strategies when source amplitude and medium attenuation are poorly known. *Journal of Glaciology*, *55*(193), 931–937. https://doi.org/10.3189/002214309790152528

Holland, P. R., Bevan, S. L., & Luckman, A. J. (2023). Strong ocean melting feedback during the recent retreat of thwaites glacier. *Geophysical Research Letters*, *50*(8), e2023GL103088. https://doi.org/10.1029/2023GL103088

Holland, P. R., Bracegirdle, T. J., Dutrieux, P., Jenkins, A., & Steig, E. J. (2019). West antarctic ice loss influenced by internal climate variability and anthropogenic forcing. *Nature Geoscience*, *12*(9), 718–724. https://doi.org/10.1038/s41561-019-0420-9

Holschuh, N., Christianson, K., Paden, J., Alley, R., & Anandakrishnan, S. (2020). Linking postglacial landscapes to glacier dynamics using swath radar at thwaites glacier, Antarctica. *Geology*, *48*(3), 268–272. https://doi.org/10.1130/G46772.1

Horgan, H. J., Anandakrishnan, S., Alley, R. B., Burkett, P. G., & Peters, L. E. (2011). Englacial seismic reflectivity: Imaging crystal-orientation fabric in west Antarctica. *Journal of Glaciology*, *57*(204), 639–650. https://doi.org/10.3189/002214311797409686

Horgan, H. J., van Haastrecht, L., Alley, R. B., Anandakrishnan, S., Beem, L. H., Christianson, K., et al. (2021). Grounding zone subglacial properties from calibrated active-source seismic methods. *The Cryosphere*, *15*(4), 1863–1880. https://doi.org/10.5194/tc-15-1863-2021

Horikawa, K., Iwai, M., Hillenbrand, C.-D., Siddoway, C. S., Halberstadt, A. R., Cowan, E. A., et al. (2026). Repeated major inland retreat of thwaites and pine island glaciers (west Antarctica) during the Pliocene. *Proceedings of the National Academy of Sciences*, *123*(1), e2508341122. https://doi.org/10.1073/pnas.2508341122

Hudson, T., Brisbourne, A., & Zoet, L. (2025). Icequake rupture suggests antarctic ice stream beds may be stronger, yet more dynamic than previously assumed. *PREPRINT (Version 1) available at Research Square*. https://doi.org/10.21203/rs.3.rs-7825540/v1

Iverson, N. R., Hanson, B., Hooke, R. L., & Jansson, P. (1995). Flow mechanism of glaciers on soft beds. *Science*, *267*(5194), 80–81. https://doi.org/10.1126/science.267.5194.80

Iverson, N. R., Jansson, P., & Hooke, R. L. (1994). In-situ measurement of the strength of deforming subglacial till. *Journal of Glaciology*, *40*(136), 497–503. https://doi.org/10.3189/S0022143000012375

Jordan, T. A., Thompson, S., Kulessa, B., & Ferraccioli, F. (2023). Geological sketch map and implications for ice flow of thwaites glacier, West Antarctica, from integrated aerogeophysical observations. *Science Advances*, *9*(22), eadf2639. https://doi.org/10.1126/sciadv.adf2639

Joughin, I., Smith, B. E., & Medley, B. (2014). Marine ice sheet collapse potentially under way for the thwaites glacier basin, west Antarctica. *Science*, *344*(6185), 735–738. https://doi.org/10.1126/science.1249055

Joughin, I., Smith, B. E., & Schoof, C. G. (2019). Regularized coulomb friction laws for ice sheet sliding: Application to pine island glacier, Antarctica. *Geophysical Research Letters*, *46*(9), 4764–4771. https://doi.org/10.1029/2019GL082526

Kamb, B. (2001). Basal zone of the West antarctic ice streams and its role in lubrication of their rapid motion. In *The West Antarctic Ice Sheet: Behavior and environment* (pp. 157–199). American Geophysical Union (AGU). https://doi.org/10.1029/AR077p0157

Kazmierczak, E., Sun, S., Coulon, V., & Pattyn, F. (2022). Subglacial hydrology modulates basal sliding response of the antarctic ice sheet to climate forcing. *The Cryosphere*, *16*(10), 4537–4552. https://doi.org/10.5194/tc-16-4537-2022

21699011, 2026, 12, Downloaded from https://agupubs.onlinelibrary.wiley.com/doi/10.1029/2026JF009300 by British Antarctic Survey, Wiley Online Library on [27/11/2026]. See the Terms and Conditions (https://onlinelibrary.wiley.com/terms-and-conditions) on Wiley Online Library for rules of use; OA articles are governed by the applicable Creative Commons License

Kirkbride, M. P. (2002). 6 - Processes of glacial transportation. In J. Menzies (Ed.), *Modern and past glacial environments* (pp. 147–169). Butterworth-Heinemann. https://doi.org/10.1016/B978-075064226-2/50009-X

Knott, C. G. (1899). Reflexion and refraction of elastic waves with seismological applications. *Philosophical Magazine*.

Koellner, S., Parizek, B. R., Alley, R. B., Muto, A., & Holschuh, N. (2019). The impact of spatially-variable basal properties on outlet glacier flow. *Earth and Planetary Science Letters*, *515*, 200–208. https://doi.org/10.1016/j.epsl.2019.03.026

Kyrke-Smith, T. M., Gudmundsson, G. H., & Farrell, P. E. (2017). Can seismic observations of bed conditions on ice streams help constrain parameters in ice flow models? *Journal of Geophysical Research: Earth Surface*, *122*(11), 2269–2282. https://doi.org/10.1002/2017JF004373

Luthra, T., Anandakrishnan, S., Winberry, J. P., Alley, R. B., & Holschuh, N. (2016). Basal characteristics of the main sticky spot on the ice plain of whillans ice stream, Antarctica. *Earth and Planetary Science Letters*, *440*, 12–19. https://doi.org/10.1016/j.epsl.2016.01.035

Luthra, T., Peters, L. E., Anandakrishnan, S., Alley, R. B., Holschuh, N., & Smith, A. M. (2017). Characteristics of the sticky spot of kamb ice stream, West Antarctica. *Journal of Geophysical Research: Earth Surface*, *122*(3), 641–653. https://doi.org/10.1002/2016JF004181

MacGregor, J. A., Catania, G. A., Conway, H., Schroeder, D. M., Joughin, I., Young, D. A., et al. (2013). Weak bed control of the eastern shear margin of Thwaites Glacier, West Antarctica. *Journal of Glaciology*, *59*(217), 900–912. https://doi.org/10.3189/2013JoG13J050

Marschalek, J. W., van de Flierdt, T., Siddoway, C. S., Thomson, S. N., Paxman, G. J. G., Jamieson, S. S. R., et al. (2025). Reconstructing eocene antarctic river drainage from provenance analysis of amundsen sea embayment sediments. *Science Advances*, *11*(50), eaea2373. https://doi.org/10.1126/sciadv.aea2373

Mavko, G., Mukerji, T., & Dvorkin, J. (2009). Seismic wave propagation. In *The rock physics handbook: Tools for seismic analysis of porous media* (2nd ed., pp. 81–168). Cambridge University Press. https://doi.org/10.1017/CBO9780511626753.004

Medwin, H., & Clay, C. S. (1998). Chapter 3 - Transmissions along ray paths. In H. Medwin & C. S. Clay (Eds.), *Fundamentals of acoustical oceanography* (pp. 70–126). Academic Press. https://doi.org/10.1016/B978-012487570-8/50005-2

Mercer, J. H. (1978). West antarctic ice sheet and CO2 greenhouse effect: A threat of disaster. *Nature*, *271*(5643), 321–325. https://doi.org/10.1038/271321a0

Metropolis, N., Rosenbluth, A. W., Rosenbluth, M. N., Teller, A. H., & Teller, E. (1953). Equation of state calculations by fast computing machines. *The Journal of Chemical Physics*, *21*(6), 1087–1092. https://doi.org/10.1063/1.1699114

Morgan-Witts, N., Hansen, D. D., Zoet, L. K., & Haseloff, M. (2025). Cyclic effective pressure loading impacts glacial slip over deformable beds. *Geophysical Research Letters*, *52*(8), e2024GL113658. https://doi.org/10.1029/2024GL113658

Mouginot, J., Rignot, E., & Scheuchl, B. (2014). Sustained increase in ice discharge from the Amundsen Sea embayment, West Antarctica, from 1973 to 2013. *Geophysical Research Letters*, *41*(5), 1576–1584. https://doi.org/10.1002/2013GL059069

Muerdter, D., Kelly, M., & Van Koughnet, R. (2005). The effect of reflector dip on AVO analysisl. *SEG Technical Program Expanded Abstracts*, *1*, 281–284. https://doi.org/10.1190/1.2144321

Muto, A., Alley, R. B., Parizek, B. R., & Anandakrishnan, S. (2019). Bed-type variability and till (dis)continuity beneath thwaites glacier, West Antarctica. *Annals of Glaciology*, *60*(80), 82–90. https://doi.org/10.1017/aog.2019.32

Muto, A., Anandakrishnan, S., Alley, R. B., Horgan, H. J., Parizek, B. R., Koellner, S., et al. (2019). Relating bed character and subglacial morphology using seismic data from thwaites glacier, West Antarctica. *Earth and Planetary Science Letters*, *507*, 199–206. https://doi.org/10.1016/j.epsl.2018.12.008

Otosaka, I. N., Shepherd, A., Ivins, E. R., Schlegel, N.-J., Amory, C., van den Broeke, M. R., et al. (2023). Mass balance of the Greenland and antarctic ice sheets from 1992 to 2020. *Earth System Science Data*, *15*(4), 1597–1616. https://doi.org/10.5194/essd-15-1597-2023

Parizek, B. R., Christianson, K., Anandakrishnan, S., Alley, R. B., Walker, R. T., Edwards, R. A., et al. (2013). Dynamic (in)stability of thwaites glacier, West Antarctica. *Journal of Geophysical Research: Earth Surface*, *118*(2), 638–655. https://doi.org/10.1002/jgrf.20044

Passchier, S., Hillenbrand, C.-D., Hemming, S., Ehrmann, W., Frederichs, T., Bohaty, S. M., et al. (2025). West antarctic ice retreat and paleoceanography in the amundsen sea in the warm early pliocene. *Nature Communications*, *16*(1), 5609. https://doi.org/10.1038/s41467-025-60772-8

Peters, L. E., & Anandakrishnan, S. (2007). Subglacial conditions at a sticky spot along kamb ice stream, West Antarctica. In *Antarctica: A keystone in a changing world - Online proceedings for the 10th international symposium on Antarctic Earth sciences*. U.S. Geological Survey. https://doi.org/10.3133/ofr20071047SRP097

Peters, L. E., Anandakrishnan, S., Alley, R. B., & Smith, A. M. (2007). Extensive storage of basal meltwater in the onset region of a major West antarctic ice stream. *Geology*, *35*(3), 251. https://doi.org/10.1130/G23222A.1

Peters, L. E., Anandakrishnan, S., Alley, R. B., Winberry, J. P., Voigt, D. E., Smith, A. M., & Morse, D. L. (2006). Subglacial sediments as a control on the onset and location of two siple Coast ice streams, West Antarctica. *Journal of Geophysical Research*, *111*(B1). https://doi.org/10.1029/2005JB003766

Pollard, D., & DeConto, R. M. (2020). Continuous simulations over the last 40 million years with a coupled antarctic ice sheet-sediment model. *Palaeogeography, Palaeoclimatology, Palaeoecology*, *537*, 109374. https://doi.org/10.1016/j.palaeo.2019.109374

Pritchard, H. D., Fretwell, P. T., Fremand, A. C., Bodart, J. A., Kirkham, J. D., Aitken, A., et al. (2025). Bedmap3 updated ice bed, surface and thickness gridded datasets for Antarctica. *Scientific Data*, *12*(1), 414. https://doi.org/10.1038/s41597-025-04672-y

Rignot, E., Mouginot, J., Scheuchl, B., van den Broeke, M., van Wessem, M. J., & Morlighem, M. (2019). Four decades of antarctic ice sheet mass balance from 1979–2017. *Proceedings of the National Academy of Sciences*, *116*(4), 1095–1103. https://doi.org/10.1073/pnas.1812883116

Rignot, E., Scheuchl, B., Barre, J.-B., Brancato, V., Charrier, L., Chen, H., et al. (2026). Thirty years of glacier grounding line retreat in Antarctica. *Proceedings of the National Academy of Sciences*, *123*(10), e2524380123. https://doi.org/10.1073/pnas.2524380123

Ritz, C., Edwards, T. L., Durand, G., Payne, A. J., Peyaud, V., & Hindmarsh, R. C. A. (2015). Potential sea-level rise from antarctic ice-sheet instability constrained by observations. *Nature*, *528*(7580), 115–118. https://doi.org/10.1038/nature16147

Röthlisberger, H. (1972). *Seismic exploration in cold regions, CRREL Monograph 11-A 2a. Hanover, New Hampshire*. Cold Regions Research and Engineering Laboratory.

Scambos, T., Bell, R., Alley, R., Anandakrishnan, S., Bromwich, D., Brunt, K., et al. (2017). How much, how fast? A science review and outlook for research on the instability of antarctica's thwaites glacier in the 21st century. *Global and Planetary Change*, *153*, 16–34. https://doi.org/10.1016/j.gloplacha.2017.04.008

Schlegel, R., Murray, T., Smith, A. M., Brisbourne, A. M., Booth, A. D., King, E. C., & Clark, R. A. (2022). Radar derived subglacial properties and landforms beneath rutford ice stream, West Antarctica. *Journal of Geophysical Research: Earth Surface*, *127*(1), e2021JF006349. https://doi.org/10.1029/2021JF006349

Schlegel, R., Zoet, L. K., Booth, A. D., Smith, A. M., Clark, R. A., & Brisbourne, A. M. (2025). Subglacial landscape formation and sediment discharge: Relating basal conditions to bedform dimensions and properties at rutford ice stream, West Antarctica. *Boreas*, *54*(4), 672–686. https://doi.org/10.1111/bor.70002

21699011, 2026, 12, Downloaded from https://agupubs.onlinelibrary.wiley.com/doi/10.1029/2026JF009300 by British Antarctic Survey, Wiley Online Library on [27/11/2026]. See the Terms and Conditions (https://onlinelibrary.wiley.com/terms-and-conditions) on Wiley Online Library for rules of use; OA articles are governed by the applicable Creative Commons License

Schmidt, B. E., Washam, P., Davis, P. E. D., Nicholls, K. W., Holland, D. M., Lawrence, J. D., et al. (2023). Heterogeneous melting near the thwaites glacier grounding line. *Nature*, *614*(7948), 471–478. https://doi.org/10.1038/s41586-022-05691-0

Schoof, C. (2005). The effect of cavitation on glacier sliding. *Proceedings of the Royal Society A: Mathematical, Physical and Engineering Sciences*, *461*(2055), 609–627. https://doi.org/10.1098/rspa.2004.1350

Schwans, E., Parizek, B. R., Alley, R. B., Anandakrishnan, S., & Morlighem, M. M. (2023). Model insights into bed control on retreat of thwaites glacier, West Antarctica. *Journal of Glaciology*, *69*(277), 1241–1259. https://doi.org/10.1017/jog.2023.13

Schwans, E., Parizek, B. R., Alley, R. B., Anandakrishnan, S., & Wang, S. (2026). Data-driven bed rheology enhances retreat on thwaites glacier. *Journal of Glaciology*, *72*, 1–21. https://doi.org/10.1017/jog.2026.10168

Seroussi, H., Nakayama, Y., Larour, E., Menemenlis, D., Morlighem, M., Rignot, E., & Khazendar, A. (2017). Continued retreat of thwaites glacier, West Antarctica, controlled by bed topography and ocean circulation. *Geophysical Research Letters*, *44*(12), 6191–6199. https://doi.org/10.1002/2017GL072910

Shuey, R. T. (1985). A simplification of the zoeppritz equations. *Geophysics*, *50*(4), 609–614. https://doi.org/10.1190/1.1441936

Smith, A. M. (1997). Basal conditions on rutford ice stream, West Antarctica, from seismic observations. *Journal of Geophysical Research*, *102*(B1), 543–552. https://doi.org/10.1029/96JB02933

Smith, A. M. (2007). Subglacial bed properties from normal-incidence seismic reflection data. *Journal of Environmental and Engineering Geophysics*, *12*(1), 3–13. https://doi.org/10.2113/JEEG12.1.3

Smith, A. M., Anker, P. G. D., Nicholls, K. W., Makinson, K., Murray, T., Rios-Costas, S., et al. (2021). Ice stream subglacial access for ice-sheet history and fast ice flow: The BEAMISH project on rutford ice stream, West Antarctica and initial results on basal conditions. *Annals of Glaciology*, *62*(85–86), 203–211. https://doi.org/10.1017/aog.2020.82

Teng, T.-L. (1968). Attenuation of body waves and the Q structure of the mantle. *Journal of Geophysical Research (1896-1977)*, *73*(6), 2195–2208. https://doi.org/10.1029/JB073i006p02195

Truffer, M., Harrison, W. D., & Echelmeyer, K. A. (2000). Glacier motion dominated by processes deep in underlying till. *Journal of Glaciology*, *46*(153), 213–221. https://doi.org/10.3189/172756500781832909

Tsai, V. C., Stewart, A. L., & Thompson, A. F. (2015). Marine ice-sheet profiles and stability under coulomb basal conditions. *Journal of Glaciology*, *61*(226), 205–215. https://doi.org/10.3189/2015JoG14J221

Tulaczyk, S., Kamb, W. B., & Engelhardt, H. F. (2000). Basal mechanics of ice stream B, West Antarctica: 1. Till mechanics. *Journal of Geophysical Research*, *105*(B1), 463–481. https://doi.org/10.1029/1999JB900329

Voigt, D. E., Peters, L. E., & Anandakrishnan, S. (2013). Georods': The development of a four-element geophone for improved seismic imaging of glaciers and ice sheets. *Annals of Glaciology*, *54*(64), 142–148. https://doi.org/10.3189/2013AoG64A432

Weertman, J. (1957). On the sliding of glaciers. *Journal of Glaciology*, *3*(21), 33–38. https://doi.org/10.3189/S0022143000024709

Wild, C. T., Alley, K. E., Muto, A., Truffer, M., Scambos, T. A., & Pettit, E. C. (2022). Weakening of the pinning point buttressing thwaites glacier, West Antarctica. *The Cryosphere*, *16*(2), 397–417. https://doi.org/10.5194/tc-16-397-2022

Wilson, D. S., Jamieson, S. S. R., Barrett, P. J., Leitchenkov, G., Gohl, K., & Larter, R. D. (2012). Antarctic topography at the Eocene–Oligocene boundary. *Palaeogeography, Palaeoclimatology, Palaeoecology*, *335*, 24–34. https://doi.org/10.1016/j.palaeo.2011.05.028

Yu, H., Rignot, E., Seroussi, H., & Morlighem, M. (2018). Retreat of thwaites glacier, West Antarctica, over the next 100 years using various ice flow models, ice shelf melt scenarios and basal friction laws. *The Cryosphere*, *12*(12), 3861–3876. https://doi.org/10.5194/tc-12-3861-2018

Zechmann, J. M., Booth, A. D., Truffer, M., Gusmeroli, A., Amundson, J. M., & Larsen, C. F. (2018). Active seismic studies in valley glacier settings: Strategies and limitations. *Journal of Glaciology*, *64*(247), 796–810. https://doi.org/10.1017/jog.2018.69

Zeising, O., Eisen, O., Hofstede, C., Agnew, R., Brisbourne, A., Hoffman, A. O., & Anandakrishnan, S. (2026). Hard rocks and deep wetlands beneath thwaites glacier in Antarctica. *Communications Earth & Environment*, *7*(1), 366. https://doi.org/10.1038/s43247-026-03502-2

Zoeppritz, K. (1919). VII b. Über Reflexion und Durchgang seismischer Wellen durch Unstetigkeitsflächen. Nachrichten von der Gesellschaft der Wissenschaften zu Göttingen. *Mathematisch-Physikalische Klasse*, *1919*, 66–84.

Zoet, L. K., & Iverson, N. R. (2020). A slip law for glaciers on deformable beds. *Science*, *368*(6486), 76–78. https://doi.org/10.1126/science.aaz1183

Zoet, L. K., Williams, K., Corum, M., Prescott, J., Le Brun, N., Stutz, J., et al. (2026). The mechanical, hydrological and mineralogic properties of 11 antarctic tills. *Journal of Glaciology*, *72*, e98. https://doi.org/10.1017/jog.2026.10208

21699011, 2026, 12, Downloaded from https://agupubs.onlinelibrary.wiley.com/doi/10.1029/2026JF009300 by British Antarctic Survey, Wiley Online Library on [27/11/2026]. See the Terms and Conditions (https://onlinelibrary.wiley.com/terms-and-conditions) on Wiley Online Library for rules of use; OA articles are governed by the applicable Creative Commons License